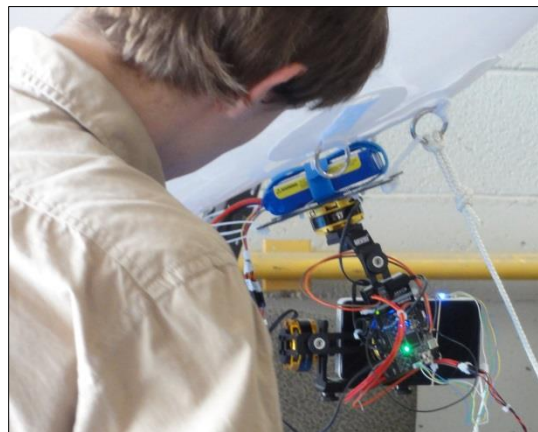


### 3.2.3 Traffic Monitoring

MTRI selected a 15 foot long tethered blimp for its testing. The blimp has a net lift of approximately 8 pounds; the camera/gimbal/battery payload weighs approximately 4 ½ pounds. It takes about half an hour to inflate the blimp, which requires approximately 290 feet cubed of helium (slightly less than one standard helium tank). Once inflated, the blimp will stay inflated with small top offs of gas almost indefinitely. Deflation takes about 20 minutes. A Samsung 4G camera was purchased to test the transmission of video from the blimp via the 4G cellular network. MTRI set up an account on USTREAM which allowed the near real time monitoring of the video stream from the camera, with only a 10-15 second delay. The video stream is saved on USTREAM which allows reviewing of the video after test flights are completed. Several flights were made from behind MTRI's offices as lab tests. The first test was done as a proof of concept to see what the view from the blimp might be. The first flights were made with a cellphone camera on a picavet hung from the blimp. While the tests were successful, the camera mounted on the picavet system could not be pointed and swung like a pendulum under the blimp which made it difficult to monitor a particular location on the ground.

A battery powered gimbal was purchased to stabilize the camera and allow the camera to be pointed at a location of interest on the ground by the ground-based person in charge (Figure 3.2.3 A). The gimbal performed its stabilization function well, keeping the camera stable and pointed at the area of interest although it did tend to drift in azimuth. This problem was traced to the limited 'trim' adjustability in the controller used to point the camera.



**Figure 3.2.3 A: Operating gimbal mounted on the blimp. Notice that while the blimp is nose up, the camera is level.**

### 3.2.4 Simultaneous Location and Mapping (SLAM)

SLAM refers to a class of algorithms that generate a map of a previously unknown environment while simultaneously tracking the vehicle's position within that map using on-board sensors

(Zhang et al., 2013). It is important to have a very accurate position estimate of the sensing platform to enable the fusion of different sensors over a large area and provide automation for capabilities such as autonomous flight and obstacle avoidance. The diversity of published theory, applications notes, and implementations is overwhelming with thousands of articles available describing various solutions given specific constraints (DARLA, [www.apl.washington.edu/project/project.php?id=darla](http://www.apl.washington.edu/project/project.php?id=darla)). The three primary constraints common to the majority of the published literature are that the environment be approximately two-dimensional (2-D), time-invariant (that is, it is relatively static over a data collection period), and contain a sufficient feature density such that multiple features be visible to the sensing platform from sequential locations along a robot's trajectory.

Existing SLAM algorithms are typically designed for applications where a LIDAR scanner is mounted to a ground based robot and is used to scan only a 2-D slice of the environment parallel to the ground. This directly satisfies the majority of the above constraints with the exception of feature density. Most indoor environments can be modeled successfully because walls, floors, and ceilings are the primary features and motion of the robot is slow enough to establish sufficient feature density. Many outdoor environments can also be represented in a 2-D map when the overall surface terrain is largely flat and there are many obstacles such as trees, light poles, and buildings in view of the LiDAR (US DOT RITA, 2013). As long as the robot does not enter a large empty room or an open field, there is usually enough feature density to maintain a good position estimate using existing SLAM algorithms.

This project is inconsistent with those constraints. By utilizing an UAV for the sensing platform, the LiDAR is no longer sensing a 2-D slice of the environment but is used to generate a full 3-D point cloud of a (possibly) unstructured environment. Because prior SLAM research was only concerned with generating 2-D maps, most UAV-based efforts kept the LiDAR parallel to the ground and many overlapping scans were taken and then aligned using a process called scan matching. The fact that the LiDAR was sensing a majority of the same features from scan to scan made this possible. In 3-D mapping, the 2-D LiDAR is not able to track motion in the direction normal to the sensing plane and cannot be used alone to provide a full 3-D position estimate. A major goal of this project is to find a method for accurately detecting out of plane motion so that the multiple slices generated by the 2-D LiDAR can be accurately fused together into a single 3-D point cloud.

We are most interested in generating 3-D point clouds of outdoor surfaces such as roads, bridge decks, and support structures. We mounted the LIDAR under the UAV and pointed it toward the ground rather than forward as is typical of ground based robots. This produces LiDAR data that is most dense directly under the UAV. To compensate for the motion of the UAV, a MEMS accelerometer and gyroscope (an IMU) were used to find the roll and pitch of the

sensor. The UAV autopilot control system is very good at maintaining a stable platform but additional sensors help in reducing noise in the resulting point clouds. Figure 3.2.4 A is an example of the waviness found in the point cloud when the IMU sensor is disabled. When the IMU sensors are enabled, the waviness should mostly disappear for flat surfaces. Use of the MEMS IMU has shown reasonably accurate results so far.

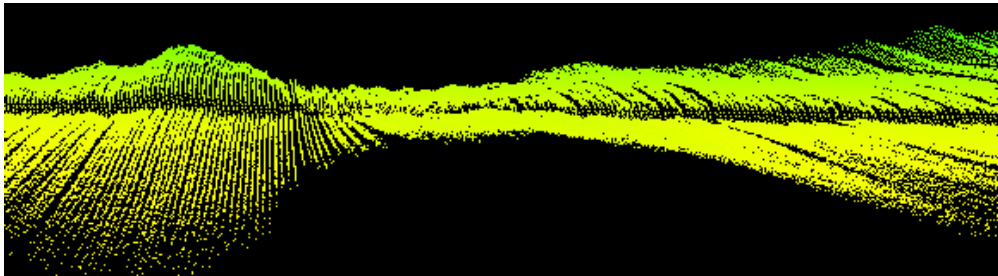
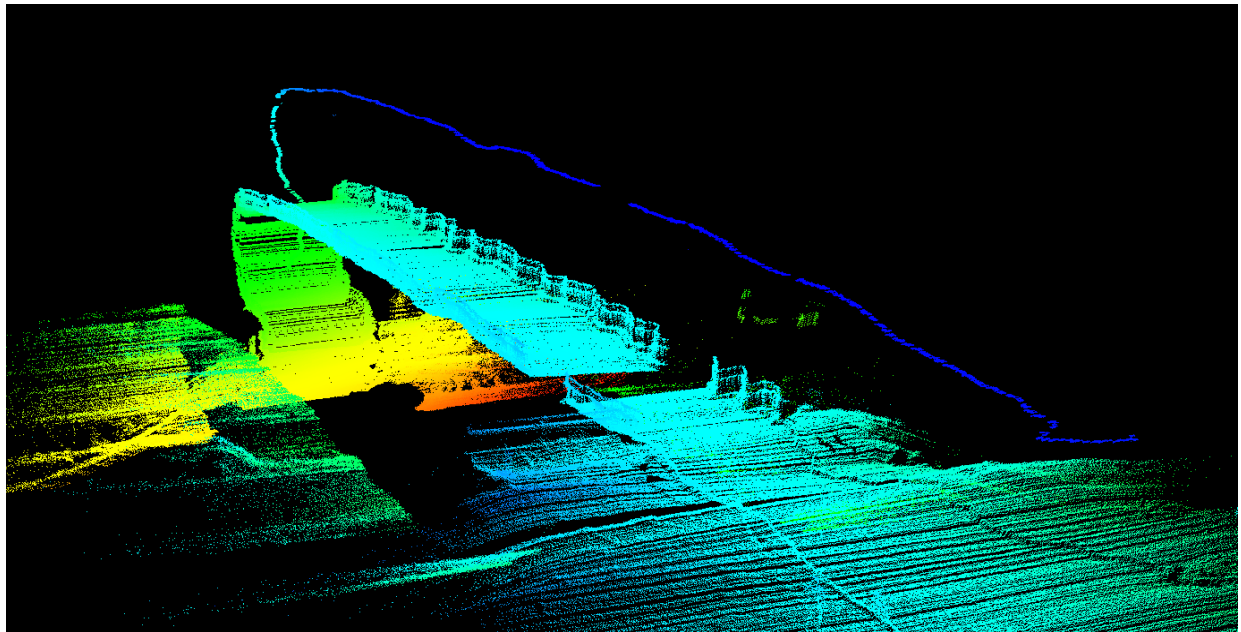


**Figure 3.2.4 A: Uncompensated platform roll and pitch waviness.**

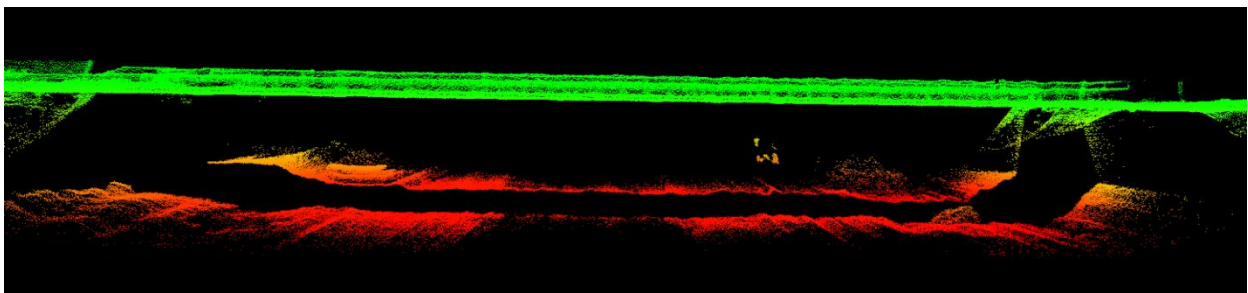
GPS can provide centimeter resolution position estimates in surveying applications where the GPS antenna remains in a fixed position while data is collected, but this is not possible on a UAV that is always under dynamic motion. Additionally, these survey grade GPS sensors are bulky and exceed the payload capacity of our UAV. Recently, Novatel started producing a lightweight high performance GNSS system that could provide an order of magnitude better position estimate using a proprietary algorithm that uses both GPS and global navigation satellite system (GNSS) constellations as well as a subscription service from TerraStar (this system uses a fixed base station with a similar configuration to differential GPS). The TerraStar subscription provides data from a global network of fixed reference stations that help model the current atmospheric conditions that affect measurement noise and produce a better position estimate. The system is expensive however, starting at \$19,000 for only the GNSS hardware. A high quality real-time radio link and TerraStar subscription service are required on top of the hardware cost. This technology may be advantageous to investigate in the near future. Additionally, our SLAM research aims to produce high-quality 3-D map data in environments where GPS signals may not be available, which decreases the expected value from such an expensive system.

Figure 3.2.4 B shows the result of generating a typical point cloud using only the raw GPS and the IMU data from the sensor platform. The altitude estimate was very poor for the first third of the bridge, but improved near the end of the bridge (this is fairly typical in GPS measurements, which have poor altitude measurement capability). The LiDAR was pointed toward the ground to provide an estimate of the altitude when the ground is approximately flat. Figure 3.2.4 C and Figure 3.2.4 D show the result of using a small region in the center of the bridge deck to estimate the sensor platform altitude.

The top view of the bridge in Figure 3.2.4 D shows that there are still some noise in the LiDAR point cloud generated from the GPS data, although it certainly looks more similar to a bridge than the raw point cloud in Figure 3.2.4 B. One of the downsides to using the LiDAR for direct altitude estimation like this is that it will only work on relatively flat surfaces. Figure 3.2.4 D does not show any arch in the bridge deck for example because it may have been removed by the LiDAR altitude estimation. The fact that the motion of the UAV is in the direction normal to the sensing plane of the LiDAR prevents direct detection of features such as surface profile in the direction of motion and is currently an open research topic for our group.



**Figure 3.2.4 B: 3-D LiDAR point cloud generation using raw GPS and IMU data.**



**Figure 3.2.4 C: Side view of bridge after using LiDAR-based altitude estimator.**

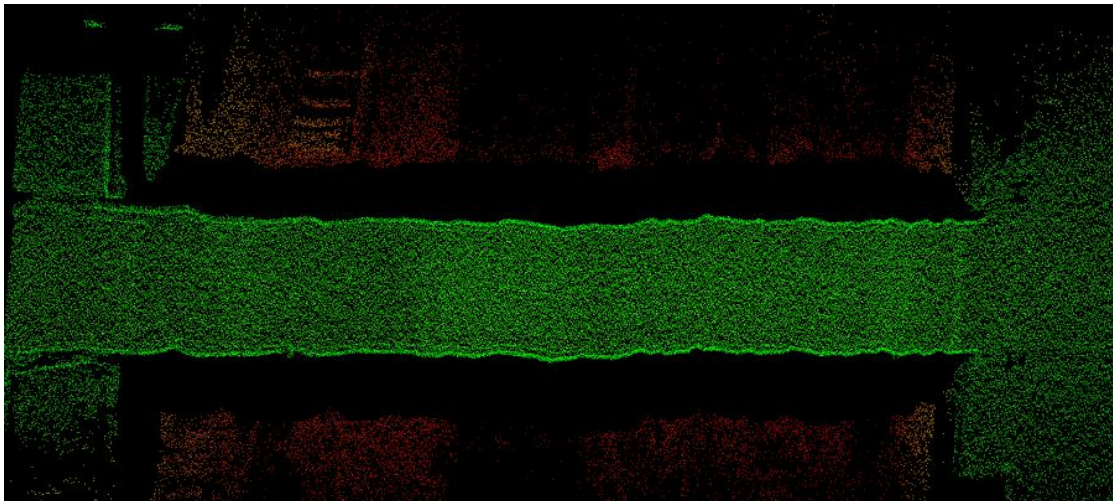


**Figure 3.2.4 D: Top view of bridge deck after using LiDAR altitude estimator.**

Further *a priori* knowledge about the environment can be used to improve the 3-D point cloud of the bridge by using bridge features such as curbs and guardrails to align the scans. This alignment process is similar to most of the published work on SLAM where features are extracted between consecutive scans and then aligned using some optimization procedure. The point cloud results of the scan matching operation are shown in Figure 3.2.4 E.

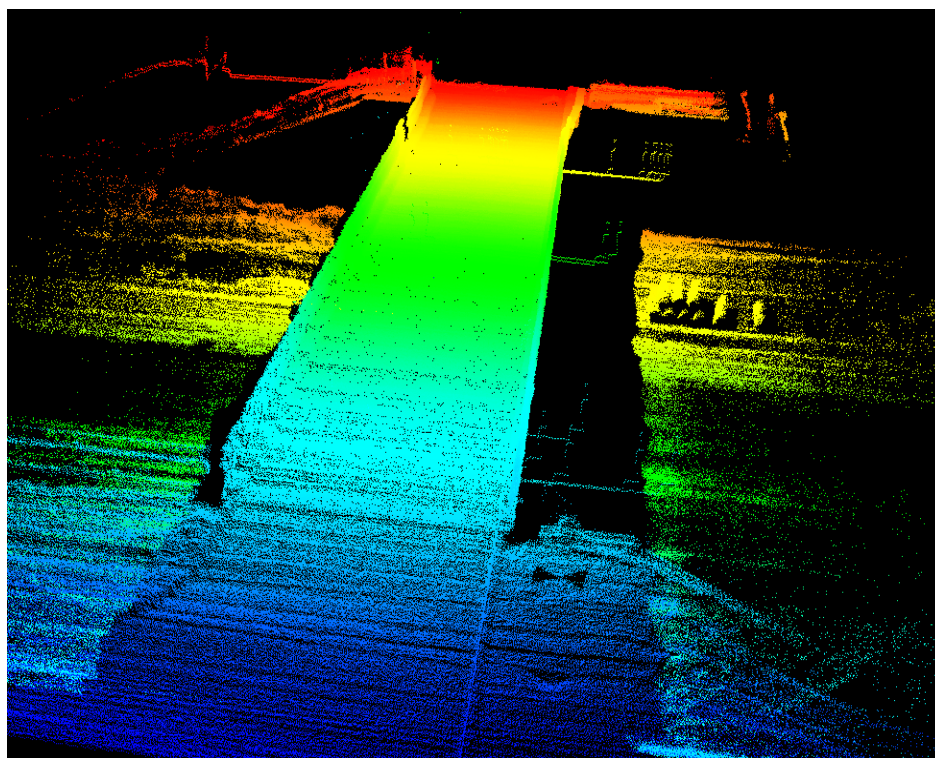


**Figure 3.2.4 E: 3-D LIDAR point cloud results after using scan-matching alignment.**

The alignment process works well for this dataset because there is a curb that runs straight through the entire bridge. This would not have worked as well if that curb was not there, and furthermore it would produce the wrong result if the curb was not relatively straight. Furthermore, GPS data is used as the truth position estimate. This can be problematic in places where GPS may be comprised, such as indoor environments. In this case, the GPS data were a good approximation of the UAV position, as the GPS data aligned well with the Google Maps satellite map of the bridge shown in Figure 3.2.4 F.

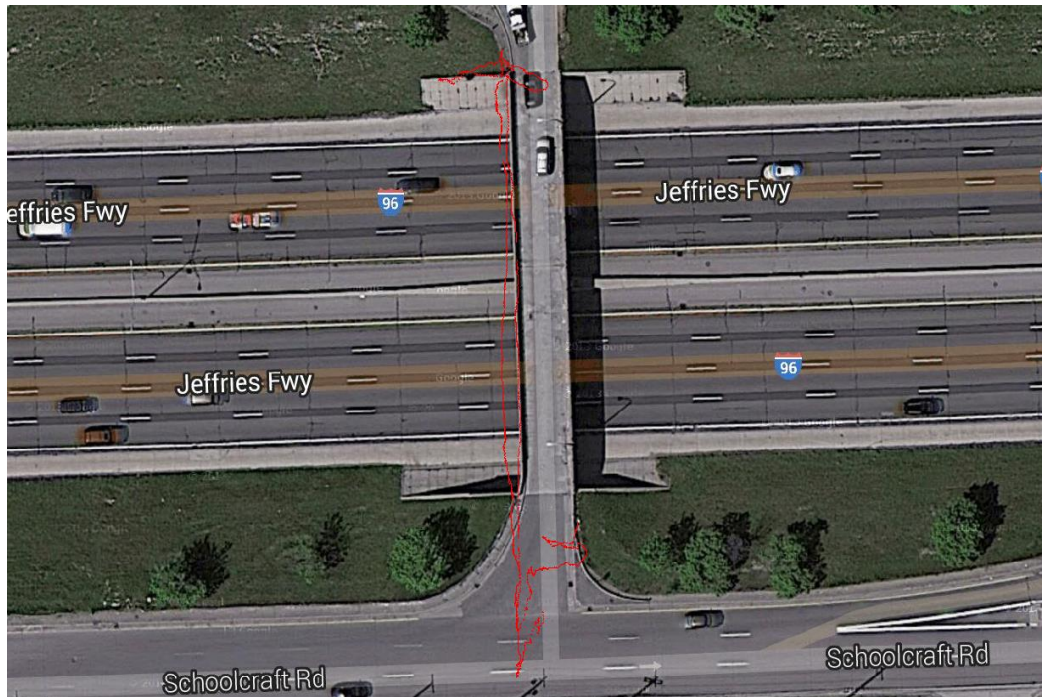


**Figure 3.2.4 F: GPS tracking over satellite image from Google Maps (red line).**

In attempt to overcome the need to rely on GPS data to provide the position estimate in the forward direction of travel, we have been investigating a number of solutions. 3-D scanning LiDAR would be one solution but existing sensors are both heavy and expensive (Pohl and Van Genderen, 1998). Velodyne is currently working on this problem and expects to release a 3-D scanning LiDAR capable of being carried on a micro-UAV platform.

The avenue we are currently focusing on to improve position estimate and point cloud accuracy is to use a camera to provide information about the motion orthogonal to the LiDAR sensing plane. By pointing a camera at the ground in addition to the LiDAR, we hope to identify and track features from frame to frame for motion tracking of the sensor platform. By fusing the LiDAR and the camera data we hope to be able to remove the scaling issues seen in camera based motion-tracking algorithms. Initially we are using both SIFT features as well as reference markers that have been added to the environment (see Figure 3.2.4 G).

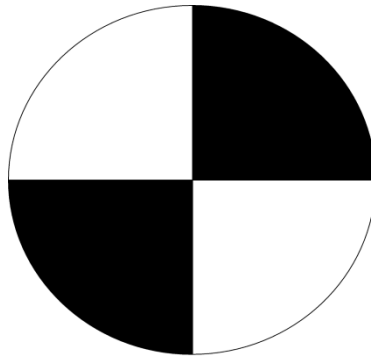


**Figure 3.2.4 G: Vision Marker**

### **3.2.5 Thermal remote sensing: instrument and methods**

#### **3.2.5.1 Thermal imaging device**

Thermal infrared remote sensing of the concrete surfaces was done with a Tau 2 uncooled core instrument (see Figure 3.2.5.1 A), produced by FLIR<sup>®</sup>. This thermal camera is sensitive to electromagnetic radiation in the spectral range of  $\sim 8$  to 15 micrometers. The model used has a 336 x 256 sensor array (pixels) of uncooled VOx Microbolometers, and a 13 millimeter (wide field of view) lens was chosen for our experiments. This gives a total field of view angles of 25 degrees x 19 degrees, and an instantaneous field of view (per pixel) of 1.3 milliradians ( $\sim 0.074$  degrees). The instrument is very compact and light (13 x 19 millimeters and  $< 70$  grams), has a low power consumption ( $\sim 1$  watt), and low power input (5 volts DC), making it ideal for meeting the requirements imposed by the UAV platform. Typical costs are around \$4,000. Full specifications and other details on the Tau 2 thermal camera can be found here:

<http://www.flir.com/cvs/cores/view/?id=54717>

The Tau 2 instrument produces digital and analog outputs in several formats. To be able to map the concrete surfaces it is necessary to capture and store individual images for further processing. Due to the size and weight constraints imposed by the UAV platform a small and lightweight solution was needed, and the TeAx ThermalCapture<sup>®</sup> module, specifically designed for the Tau 2 instrument was chosen for this purpose (see Figure 3.2.5.1 A). The ThermalCapture module captures and stores the thermal image frames from the Tau 2 sensor array in a local USB memory, as 14 bit binary files, at rates up to  $\sim 1.2$  frames per second and also costs around \$4,000. The low weight (45 grams), size (60 x 54 x 15 millimeters), and power consumption ( $\sim 2$  watts @ 5 volts DC) makes this module suitable for the UAV platform. More information on the ThermalCapture module can be found here:

<http://www.teaxtec.de/index.php?id=23&L=1>

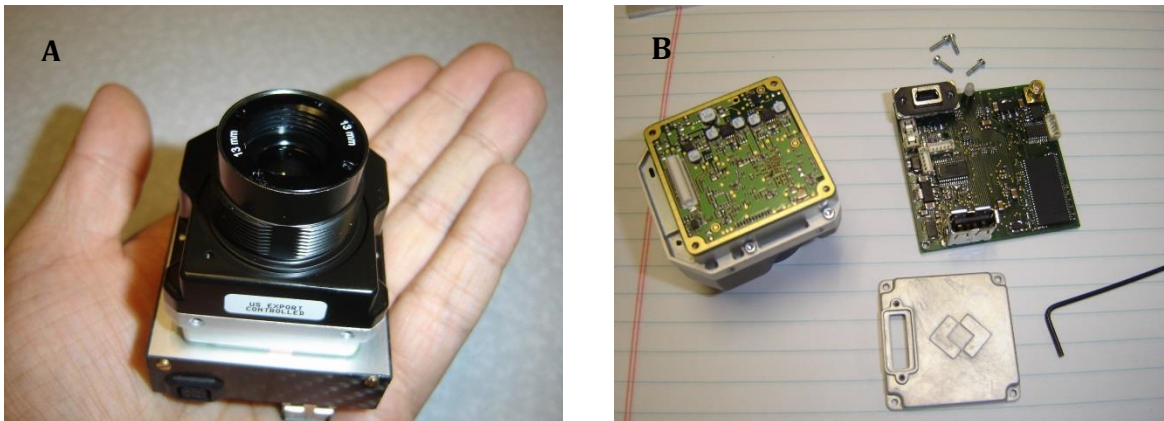


Figure 3.2.5.1 A: Tau 2 FLIR<sup>®</sup> camera and ThermalCapture TeAx<sup>®</sup> module. A Front of the camera showing the Tau 2 core, and B, ThermalCapture module being assembled and attached to the Tau 2 core.

An EasyAcc<sup>®</sup> Xtra 12000 milliampere-hour power bank battery was used to power the system. The battery has a USB (5 volts DC, up to 2.1 amps) interface that can be connected directly to the Tau 2 + ThermalCapture system, and lasts > 1 hour when fully charged. The battery pack is relatively light (320 grams), considering the charge provided, and is also relatively compact (14.2 x 7.3 x 2.3 centimeters). Smaller battery devices could also be considered if less charge (i. e. less system operation time) is needed, to reduce the weight and dimensions of the system, e.g. for extending the UAV flight time.

### 3.2.5.2 Concrete slab heating experiments

A series of controlled laboratory experiments was performed to test the performance of the Tau 2 and ThermalCapture thermal camera system for mapping concrete delaminations, and compared to a temperature calibrated FLIR<sup>®</sup> camera. To assess the effect of delaminations at different depths three concrete slabs were built, with delaminations simulated by leaving Styrofoam pieces embedded in them. The design of the concreted slabs and the simulated delaminations can be seen in Figure 3.2.5.2 A.

As previously described in Section 3.1.1, the effect of delaminations on the thermal signature is to increase the surface temperature over the areas of the delaminations, in that way the delaminations will show up as hotter areas in the thermal imagery. The Tau 2 thermal camera is not temperature calibrated, the sensor array output voltage (and the value of the digital counts recorded in the image frame files) responds linearly to the incident radiance, which in turn scales to the 4<sup>th</sup> power of absolute temperature of the emitting surface, assuming that the surface is Lambertian and behaves as a gray body, following Planck's radiation law (Jensen, 2007). Although it is possible to calibrate the digital counts output from the thermal camera and convert them to brightness temperature, this is not necessary for the purpose of mapping delaminations, as only the relative differences of the pixel radiances are needed to spatially

define the limits of the hot areas, and infer the extent of the delaminations. A series of temperature calibration experiments was performed (see Section 9.3), but this was only for the purpose of testing the general performance of the system. For the rest of the tests and measurements we performed in the project we only used the direct digital counts output from the thermal camera system, and those are as well the values reported here.

Simulated delaminations were located at 1, 1.5, and 2 inches from the surface, although some variability and errors are probably being introduced in the process of pouring the concreted in the slab casts. Four of the simulated delaminations were 4 x 4 inches in area, and located at the center of the slab was 1 x 1 inches in area. All the simulated delaminations were 3/8 of an inch thick. The heat conducting properties of the Styrofoam are expected to be close enough to those of air trapped in real delaminations, for this simulation to be valid.

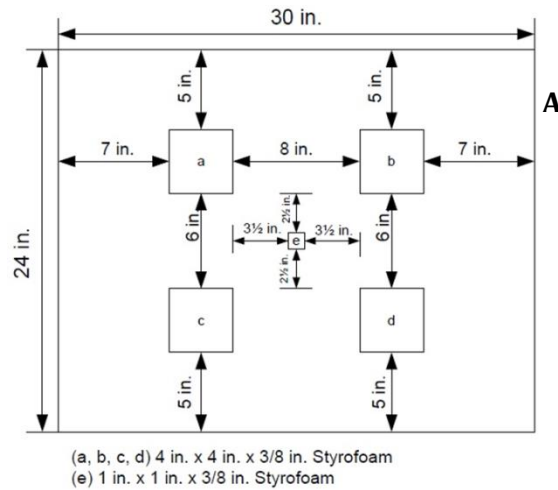


**Figure 3.2.5.2 A: A Concrete slab and simulated delaminations design (Design and drawing by K. Vanghefi) being made at Michigan Tech. B Styrofoam pieces locations in the slab molds before pouring the concrete, compare with the design in part A.**

After curing and hardening of the concrete for > 28 days, a series of heating experiments were undertaken. The slabs' concrete surface was heated with an infrared radiation lamp for 15 minutes, and then the heating lamp was turned off, allowing the slab surface to slowly cool

down. Above ambient temperatures were still measurable 45 minutes after turning off the heat lamp. A temperature calibrated FLIR<sup>®</sup> SC 640 camera was also co-located with the Tau 2 camera, acquiring images at higher frame rate. A detailed description of the experimental procedure and the details of the equipment setup can be found in Vaghefi (2013).

Unfortunately, the smooth surface of the concrete slabs reflected part of the incident infrared radiation emitted by the heating lamp, invalidating the radiance and temperature measurements. For this reason only the radiance and temperature measurements from the cooling period (after the infrared lamp was turned off) are used in our laboratory experiment.

Both the Tau 2 and the more expensive SC 640 (about \$40k) cameras produced radiance and temperature maps that highlighted the delaminations as hotter areas (see Figure 3.2.5.2 B). The performance in discriminating such areas is dependent on many factors, and in the case of our experiment, it is strongly sensitive to the delamination depth and the temperature of the concrete surface after being heated; i.e. the capacity of the thermal maps to discriminate the delamination areas is best as the concrete surface reached the maximum in temperature, right after turning off the heating lamp (~ 15 minutes into the experiment), and for the cases of the shallower (1 inch) delaminations. At higher temperatures the radiance contrast between the delamination and the background is also higher, making it easier to recognize such features. This is clearly reflected in Figure 3.2.5.2 B, and is in agreement with the theory and experimental work described in the relevant literature (see for instance Washer et al. 2009, and references therein).

The performance of the FLIR SC 640 thermal camera for detecting delaminations has been investigated and described previously (see for instance Vaghefi et al. 2013), and our laboratory experiments show that the Tau 2 has a slightly reduced but comparable sensitivity, despite the direct output being in raw digital counts (linearly scalable with radiance) instead of temperature (e.g. see Figure 3.2.5.2 B). The raw Tau 2 output images also show a strong high frequency noise component compared to the calibrated temperature output from the FLIR SC 640, but this can be mitigated by adequate post processing and filtering techniques. Figure 3.2.5.2 C shows the results of filtering the raw Tau 2 output images with different types of filters, to reduce the high frequency noise.

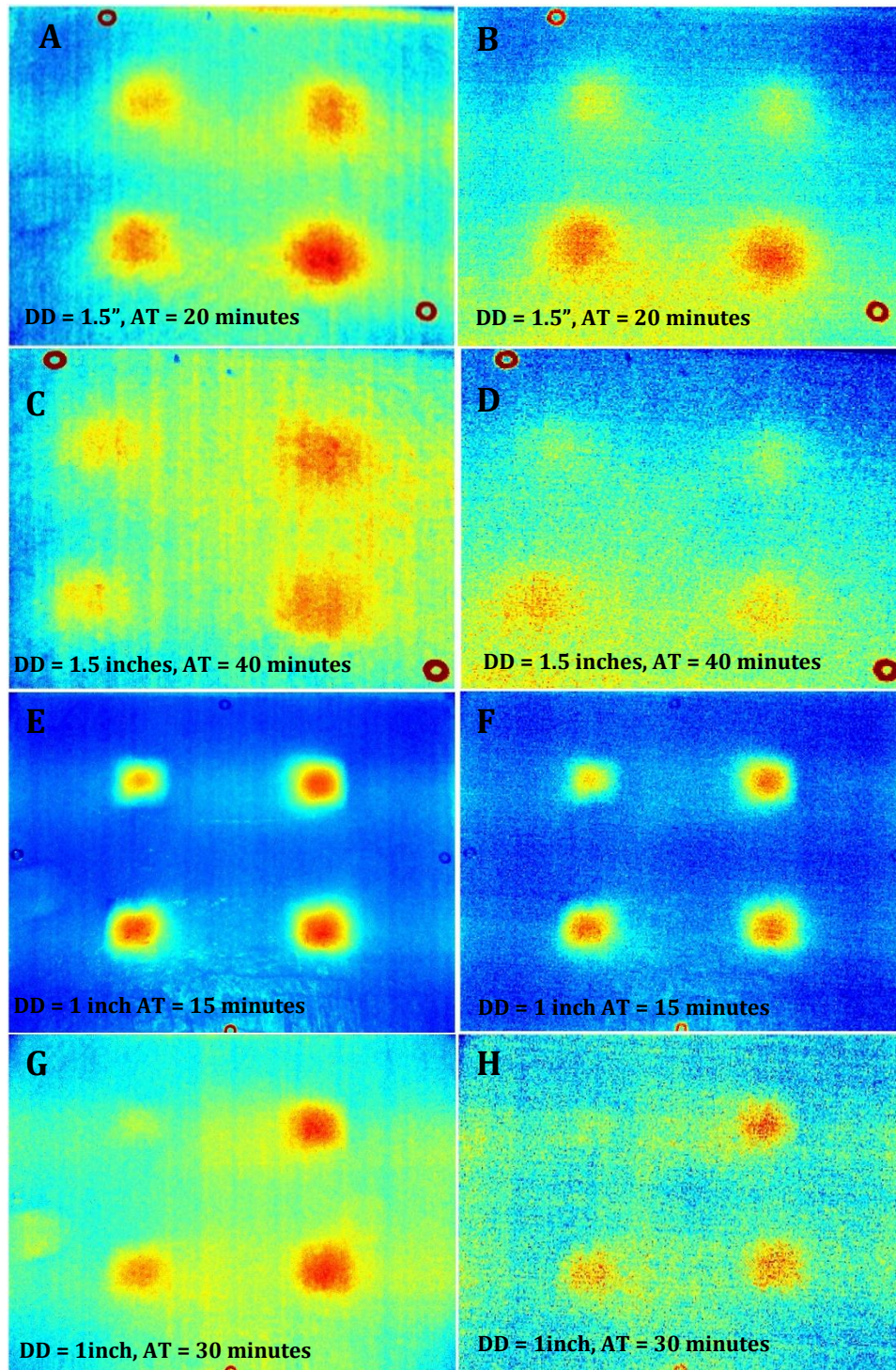
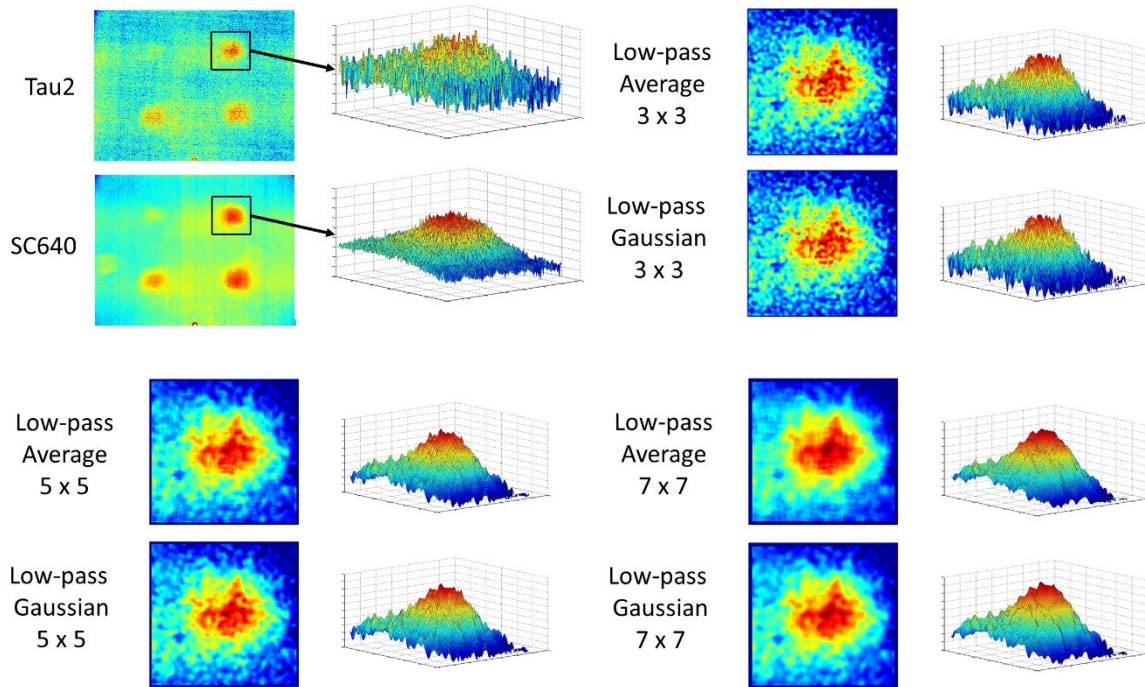


Figure 3.2.5.2 B: Comparison between FLIR SC 640 (left column) and Tau 2 (right column) cameras. Delamination Depths (DD) and image Acquisition Times (AT) (after turning off the IR lamp) are noted on each image.



**Figure 3.2.5.2 C: Effects of noise reduction through image filtering. A Comparison between the noise levels of the Tau 2 and the SC 640 cameras. B through D, smoothing effects of applying low-pass filters (average and Gaussian) with different window sizes to an example delamination from the Tau 2 dataset.**

### 3.2.6 Delamination mapping and area quantification methods

Delamination mapping and area quantification can be considered fundamentally as a binary classification problem, in which each pixel in the image is classified as either belonging or not to a delamination area. Potentially the simplest way to perform such a classification would be to visually inspect the thermal images, noting areas that appear hotter compared to their surroundings, and manually annotate them in the image, by drawing polygons that enclose them. This is one way the problem has been approached (see for instance Washer et al. 2009 and references therein), and it may meet the needs of some users, but it has some limitation and shortcomings.

The visual inspection and manual annotation method requires a well-trained operator, who can correctly discriminate between delamination and non-delamination areas, based on familiarity and training on thermal imagery, and calibration and comparison with other methods (e.g. hammer sounding or chain dragging), and the method will ultimately be very subjective and sensitive to different operators criteria. The visual method may also be very resource intensive for applications involving large and complex areas.

From the cases analyzed in our laboratory experiment it is apparent that a mapping of the delaminations by the visual inspection method would hardly reproduce the set of defined rectangles that correspond to the simulated delaminations (e.g. Figure 3.2.6 A). Visually, the higher temperature areas appear to have a smoother boundary, and in the case of the smaller 1 inch x 1 inch delamination are not visible at all. As discussed previously, the shallower delaminations that were imaged at higher temperature (e.g. at a shorter period after having been heated by the IR lamp) are easier to recognize visually and would probably have a better chance of being classified closer to their real extend by an operator performing a visual classification. In contrast, the deeper delaminations imaged at lower temperature would be harder to define with accuracy, and at some point would not be noticed anymore.

Alternatively to the visual inspection and classification, there are several automatic classification methods that can also be applied to the mapping of delaminations. In its simplest form, an automated method would rely on a threshold value of radiance (or temperature) above which the pixels would be classified as belonging to a likely delamination area. A single threshold can be chosen for an entire image, but such a general threshold method may be very limited in adapting to the local changes in the temperature background, and the emissivity changes caused by variations in the surface material.

The threshold can instead be chosen with respect to a local neighborhood of pixels, for each pixel, such a moving neighborhood or window can be chosen to be of any shape or size (within the constraints of the total image size), depending on whether the emphasis is on a more local or regional level of variation, etc. The choice of the threshold itself is also dependent on various criteria, but is usually related to the deviation above a statistical centrality measure of the distribution of values within the moving window, representative of the “background” values, e.g. the threshold can be defined as a number of standard deviation above the window mean or median, or directly as a percentile value of the distribution. And even after defining a threshold type, it is necessary to choose the actual threshold level, e.g. how many standard deviations above the mean, or what percentile is chosen as the threshold value. This choice is somewhat arbitrary, but it should be calibrated with independent delamination data (e.g. hammer or chain drag soundings) to obtain realistic results.

Figure 3.2.6 A shows the application of several of the criteria outlined here to an example image from one of our field tests sites (see Section 4.1.1 for more details on the field test experiments). As one would expect, an increase in the threshold value reduces the area classified as delaminations. The local moving window threshold methods also seem to perform better than the general threshold ones, by capturing the actual delaminations (established from hammer soundings) and avoiding other non-delaminated areas that were erroneously included

by the general thresholding method. A local percentile threshold criterion is used for the rest of the analysis performed in our research and described herein.

To assess the performance of the binary classification methods and the factors that may impact such performance, receiver operating characteristic (ROC) curves were generated for different threshold levels. ROC curves are a general tool that can be used to assess the performance of the classification methods, and make comparisons between them (see for instance Fawcett, 2006, and references). Figure 3.2.6 B shows the ROC curves for moving window percentile threshold classifiers, applied to the thermal imagery from a series of laboratory concrete slab experiments, and Table 3.2.6 A summarizes the main parameters for the curves and for specific points chosen along them.

Variations in the environmental variables and slab conditions, like surface heating (*i.e.* time since the IR lamp source was turned off) and depth of the simulated delamination, play a large role in the performance of the classifiers as has been described before in this section, but the choice of method parameters, like the moving window size, can also have a large impact in the method performance. The area under the curve (AUC) ROC curve, measures the general performance of the classifier, from 0.5 for a completely random (non-informative at all) classifier, to 1 for a perfect (0 false positive rate and 1 true positive rate) classifier. It is observed from Figure 3.2.6 B that AUC values increase with higher slab temperatures and shallow delamination depths, but also are larger for bigger window sizes for the classification algorithm. This highlights that the performance of the method relies not only on the adequate field conditions in which the measurements were performed, but also on the optimal choice of algorithm parameters for the analysis.

It is important to keep in mind that apparent radiance or brightness temperature variations do not necessarily reflect the locations of delaminations. Under the ideal conditions of our laboratory experiment the correspondence was very much straightforward and that assumption is very reasonable, but in the complex environment of an actual bridge deck, there are other factors that could lead to apparently high temperature or radiance areas that do not correspond to delaminations. An example of this will be presented, analyzed and discussed in Section 4.1.2. Finally, it is important to notice that no method solely based on remote sensing can unequivocally detect and classify delaminations with absolute certainty. Remote sensing data have to be validated and calibrated, as much as practically possible, by other indirect (*e.g.* hammer soundings, chain dragging, etc.) or even better, direct (*e.g.* coring) methods.

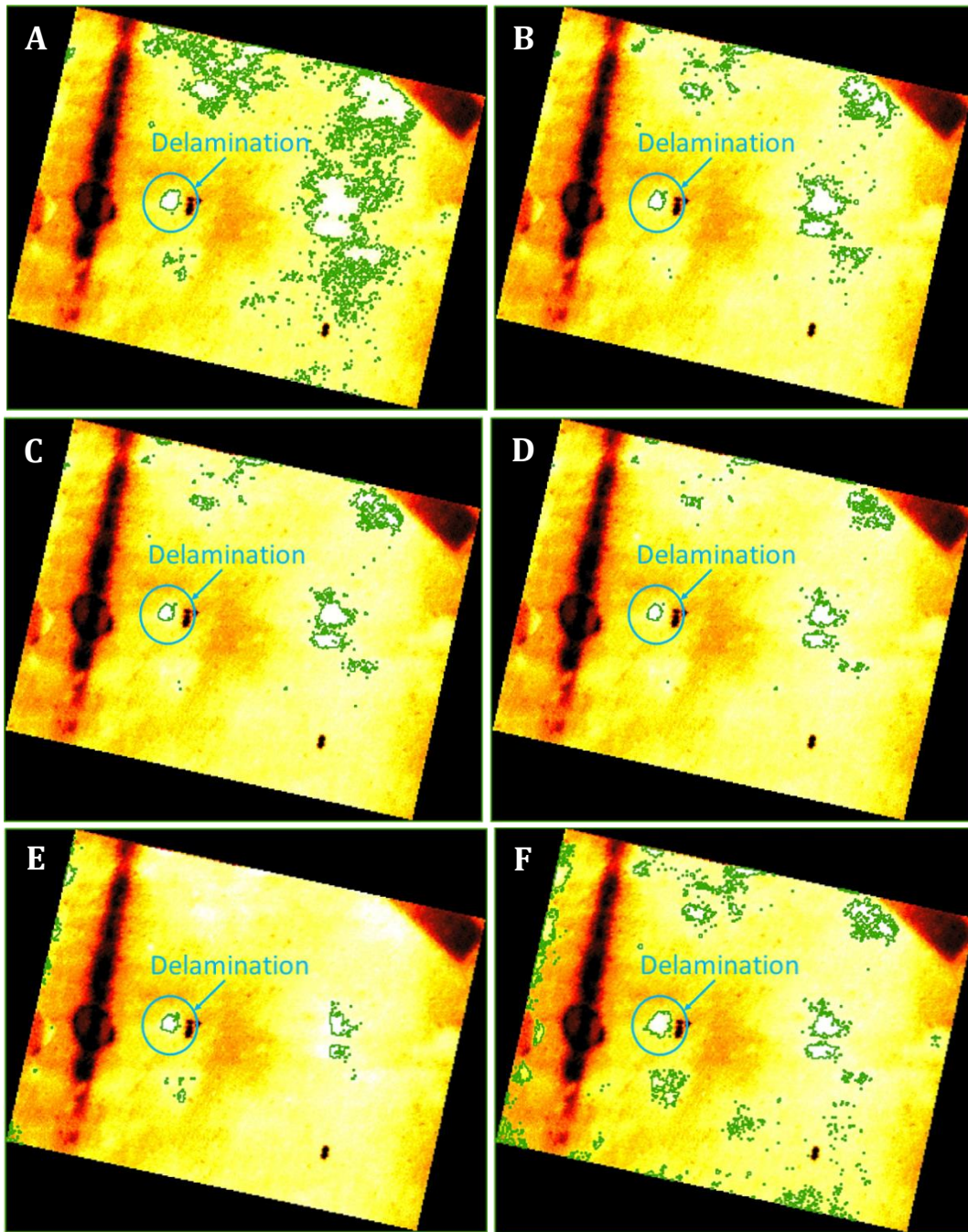
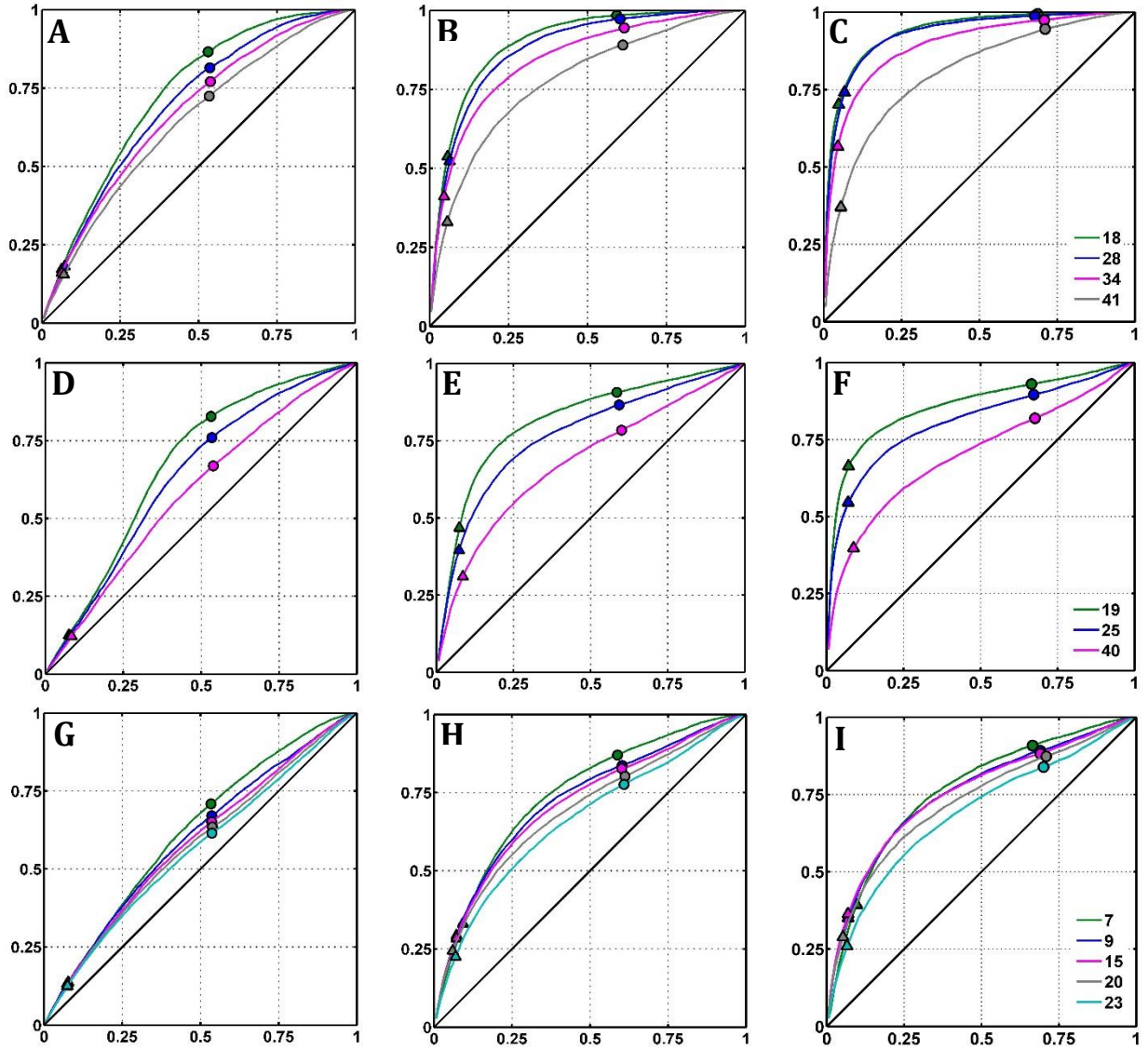


Figure 3.2.6 A: Delamination mapping (delimited by green polygons) using different algorithms and threshold criteria. A through D correspond to a single threshold classification for the whole 8 bit (0 – 255 values range) image, thresholds being respectively 255, 240, 245, and 250 units. E was derived using a 100 x 100 pixel moving window and a threshold of 2 standard deviations above the mean. F was derived also with a 100 x 100 pixel moving window and a 90<sup>th</sup> percentile threshold.



**Figure 3.2.6 B: ROC curves for the laboratory concrete slab experiments. Each row of graphs represents a different delamination depth: A, B, and C are 1 inch deep, D, E, and F are 1.5 inches deep, and G, H, and I are 2 inches deep. Each column of plots represent a different window size for the local threshold analysis: A, D, and G, resulted from a 50 x 50 pixel window, B, E, and H correspond to 100 x 100 pixel windows, and C, F, and I correspond to 150 x 150 pixel windows. The color codes of the curves correspond to the time in minutes for the acquisition of the thermal image, after powering off the heating lamp; color codes are the same for the three graphs on each row (therefore color codes are only given on the rightmost plot). Circles and triangles in each plot mark the 50<sup>th</sup> and 90<sup>th</sup> percentile threshold points, for which the parameters are also given in Table 3.2.6 A. Note how classifier performance degrades with deeper delaminations, smaller analysis windows, and longer times after heating (lower slab temperatures).**

**Table 3.2.6 A: ROC curve parameters for the laboratory concrete slab experiments. D is the delamination depth in inches. W is the analysis window width in pixels. T is the time in minutes of acquisition of the thermal image since the IR lamp was shot down (a proxy for cooling). AUC is the area under the ROC curve. FPR<sub>50</sub>, TPR<sub>50</sub> and Accu<sub>50</sub> are the false positive rate, true positive rate, and overall accuracy at a threshold of 50<sup>th</sup> percentile. FPR<sub>90</sub>, TPR<sub>90</sub> and Accu<sub>90</sub> are the false positive rate, true positive rate, and overall accuracy at a threshold of 90<sup>th</sup> percentile.**

D	W	T	AUC	FPR <sub>50</sub>	TPR <sub>50</sub>	Acc <sub>50</sub>	FPR <sub>90</sub>	TPR <sub>90</sub>	Acc <sub>90</sub>
1	50	18	0.73	0.53	0.87	0.49	0.06	0.17	0.89
1	50	28	0.70	0.54	0.82	0.49	0.07	0.18	0.88
1	50	34	0.67	0.54	0.77	0.48	0.06	0.16	0.89
1	50	41	0.64	0.53	0.72	0.48	0.07	0.15	0.88
1	100	18	0.90	0.59	0.98	0.44	0.06	0.54	0.92
1	100	28	0.88	0.60	0.97	0.43	0.06	0.52	0.91
1	100	34	0.84	0.62	0.94	0.42	0.05	0.41	0.92
1	100	41	0.78	0.61	0.89	0.42	0.06	0.33	0.91
1	150	18	0.94	0.69	0.99	0.36	0.05	0.70	0.94
1	150	28	0.93	0.68	0.99	0.36	0.07	0.74	0.92
1	150	34	0.89	0.71	0.97	0.33	0.05	0.57	0.93
1	150	41	0.80	0.71	0.95	0.33	0.06	0.37	0.91
2	50	7	0.62	0.53	0.71	0.49	0.08	0.14	0.85
2	50	9	0.60	0.54	0.67	0.48	0.07	0.13	0.85
2	50	15	0.59	0.54	0.65	0.48	0.08	0.13	0.85
2	50	20	0.57	0.54	0.63	0.48	0.07	0.12	0.85
2	50	23	0.56	0.54	0.62	0.48	0.08	0.13	0.85
2	100	7	0.75	0.59	0.87	0.45	0.09	0.33	0.86
2	100	9	0.72	0.60	0.84	0.44	0.07	0.29	0.87
2	100	15	0.71	0.60	0.83	0.44	0.07	0.28	0.87
2	100	20	0.69	0.61	0.80	0.43	0.06	0.24	0.88
2	100	23	0.66	0.61	0.78	0.43	0.07	0.23	0.87
2	150	7	0.76	0.66	0.91	0.39	0.10	0.39	0.86
2	150	9	0.75	0.69	0.89	0.36	0.07	0.35	0.88
2	150	15	0.75	0.69	0.88	0.36	0.07	0.36	0.88
2	150	20	0.73	0.71	0.87	0.34	0.05	0.29	0.89
2	150	23	0.69	0.70	0.84	0.35	0.07	0.26	0.87
1.5	50	19	0.68	0.53	0.83	0.50	0.08	0.12	0.85
1.5	50	25	0.64	0.53	0.76	0.49	0.08	0.12	0.85
1.5	50	40	0.59	0.54	0.67	0.48	0.08	0.12	0.84
1.5	100	19	0.82	0.58	0.91	0.46	0.07	0.47	0.88
1.5	100	25	0.77	0.59	0.87	0.45	0.07	0.40	0.88
1.5	100	40	0.68	0.60	0.78	0.43	0.09	0.31	0.86
1.5	150	19	0.86	0.67	0.93	0.39	0.07	0.66	0.90
1.5	150	25	0.81	0.67	0.90	0.38	0.07	0.55	0.90
1.5	150	40	0.70	0.68	0.82	0.37	0.09	0.40	0.87

#### 4. Field Demonstrations & Results

Upon determining which specific types of technologies (optical, thermal, and LiDAR), UAV platforms (hexacopter, quadcopter, and blimp/aerostat), and sensors (Nikon D800, FLIR Tau-2, Hokuyo LiDAR, Phantom 2 camera, and Samsung 4G Galaxy camera) were required to collect data, the project team tested each UAV system in an example environment based on which type of transportation purpose each system served. The hexacopter based UAV platform with optical, thermal, and LiDAR sensors were evaluated by flying over two bridges in southeast Michigan. Additionally, the micro-quadcopters used for confined space inspection demonstration were flown in two freeway pump stations located in Southfield, Michigan and in a culvert provided by the Road Commission for Oakland County. Lastly, the blimp/aerostat capabilities were demonstrated in Ann Arbor, Michigan along US Highway 23 and during a major conference. Data and initial results stemming from these demonstrations are described in detail in the following sections.

##### 4.1 Bridge Inspection – I-96 Fix bridges

Interstate-96 is a major freeway system and connects eastern (Detroit) Michigan to western (Muskegon) Michigan. The eastern section of the expressway in Wayne County was opened in 1971 and serves as a major access to Detroit from the city’s surrounding western metropolitan area. Since opening to traffic, the expressway had not experienced any major reconstruction projects and therefore was exhibiting major roadway distress. Due to the interstate’s poor condition, MDOT conducted a major reconstruction project stretching from Newburgh to Telegraph roads, and encompassed two suburban cities; Livonia and Redford (Figure 4.1 A). Through input of the public’s opinion, the interstate was completely shut down for six months from late-March through late-September. During this construction project, which became known as “96 Fix”, seven miles of road, 37 overpasses (bridges), and 24 entrance/exit ramps were either completely replaced or updated, costing approximately \$148 million dollars ([www.96fix.com](http://www.96fix.com)).



Figure 4.1 A: Seven mile stretch of Interstate-96, which was completely shut down for reconstruction.

In order to conduct tests of UAV systems and technologies, example study bridges near southeast Michigan were searched for. In-the-field test flights of any UAV system are currently best conducted where public interaction and disruption can be kept minimal, and where safety can be maximized. The ideal location and bridge will include a site with minimal traffic on the bridge and the surroundings, and minimal to complete absence of nearby overhead electrical wiring or obstacles. Through coordination with MDOT and with project team members' firsthand knowledge of the construction project and area, example study bridges, which were included in the I-96 Fix 37 bridge group scheduled for either repair or complete replacement, were selected for field data collections. Two overpass bridges in Livonia, Merriman (East U-turn) (Structure: 11515) (Figure 4.1 B) and Stark roads (Structure: 11491) (Figure 4.1 C) were selected for further analysis due to the fact that both bridges showed signs of significant distress (i.e. spalling and cracking), reconstruction efforts had not started on either bridge, and traffic below each bridge was limited to construction equipment. Additionally, MDOT Engineer Sean Kerley was successfully able to coordinate short-term traffic closures on these bridges. Therefore, all of the desired conditions were met and UAV data collections were able to be conducted.



**Figure 4.1 B: Merriman East U-turn Bridge selected for a UAV assessment.**



**Figure 4.1 C: Stark Road Bridge selected for UAV assessment.**

#### 4.1.1. Results / Integration / Analysis

On June 6, 2014, the Merriman East U-turn Bridge was assessed. During this assessment, multiple types of technologies and UAVs were used to detect different types of distress features (i.e. spalls and delaminations) on the bridge deck and underneath the bridge, and to better understand the condition of the bridge. The optical system, which uses an off-the-shelf digital single-lens reflex Nikon D800 camera system, was flown over the bridge and collected overlapping imagery at a frame rate of two images per second (Figure 4.1.1 A). The collected optical imagery was placed into a three-dimensional imagery reconstruction program, Agisoft Photoscan, to create sub-centimeter 3-D models of the bridge deck to help locate distress features such as spalls (potholes). The merged product is a high-resolution (2.5 millimeters or 1/10 inch resolution) orthorectified image, with visible spalls and patchwork (Figure 4.1.1 B). Additionally, a bridge deck 3D surface model (i.e., DEM) was also produced by Agisoft Photoscan and was used for the spall algorithm. The DEM is processed through the spall algorithm to detect minor (defined) differences in elevation, which was created to automatically detect and quantify the amount of spalling on the bridge deck. For the Merriman East U-turn Bridge, it was determined that a total area of 150.0 square feet of the bridge deck was spalled, which equates to 4.4 percent (Figure 4.1.1 C). The algorithm does not detect all of the patching on the bridge's surface, resulting in a lower spalled area than if this was included – but as patched areas are not usually included in spalling amounts, this is the correct result. Lastly, the DEM also aided in the creation of a hillshade image, or a surface with a 3-D “look” familiar to most people. This creates a visual height difference output that aids in quick differentiation between the bridge deck and spalls (Figure 4.1.1 D).

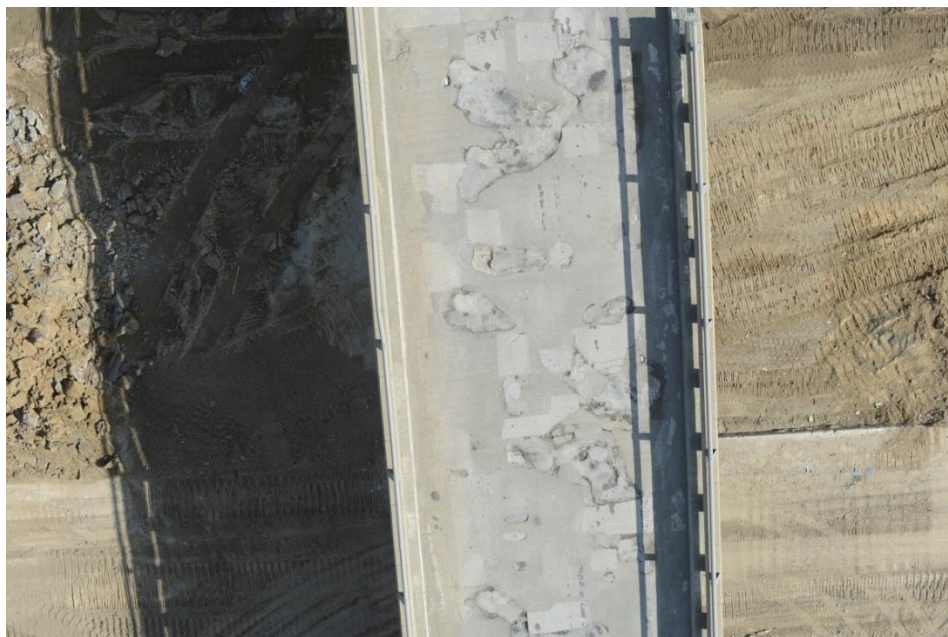


**Figure 4.1.1 A: High-resolution image of Merriman Road East U-turn Bridge.**



**Figure 4.1.1 B: Full bridge length (left) high-resolution orthorectified image of Merriman East U-turn Bridge with zoomed-in northern (middle) and southern (right) sections.**



**Figure 4.1.1 C: Automatically detected spalls on the Merriman Road East U-turn Bridge. These totaled 150.0 square feet of the bridge deck, or 4.4 percent of the total deck area.**

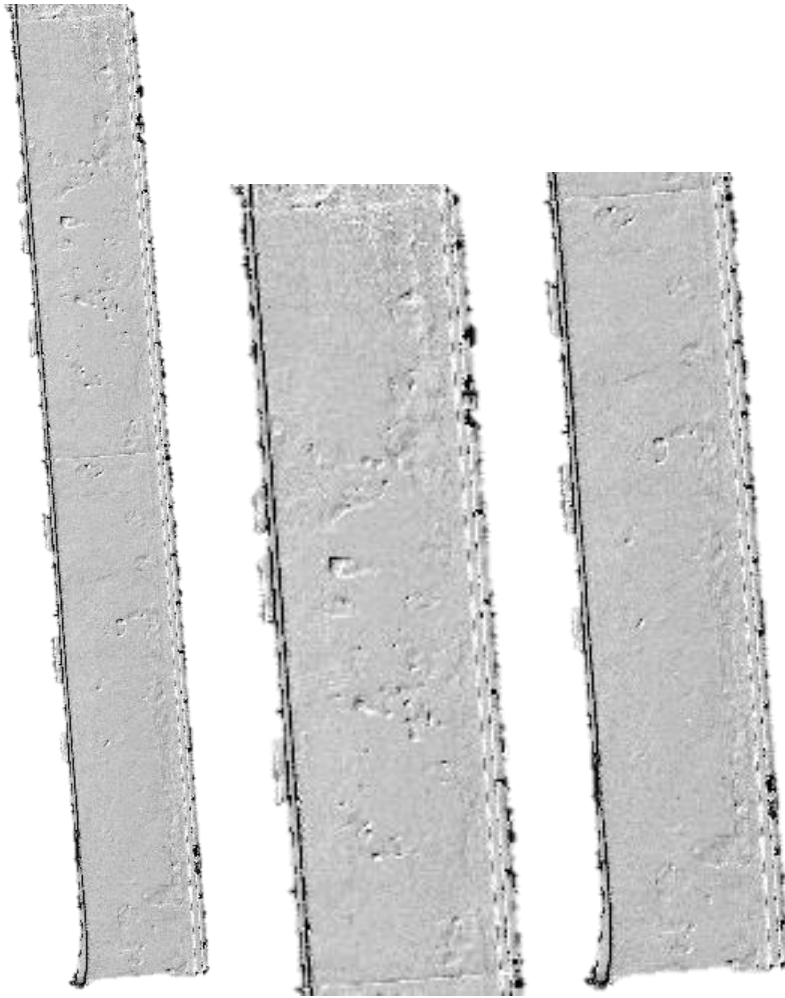


**Figure 4.1.1 D: Full bridge length (left) hillshade image of Merriman East U-turn Bridge with zoomed-in northern (middle) and southern (right) sections.**

On June 9, 2014, the bridge on Stark Road was assessed. This test incorporated the same UAV platforms, sensors, technologies, and methodologies as used during field tests conducted at the Merriman Road location except the LiDAR sensor was not flown during this assessment. After processing the collected optical imagery in Agisoft Photoscan, a high-resolution orthorectified image was produced, with clearly visible spalls and patchwork (Figure 4.1.1 E and 4.1.1 F). Lastly, the DEM also aided in the creation of a hillshade image. This created a visual height difference output that aids in quick differentiation between the bridge deck and spalls (Figure 4.1.1 G).



**Figure 4.1.1 E: High-resolution image of Stark Road Bridge.**



**Figure 4.1.1 F: Full bridge length (left) high-resolution orthorectified image of Stark Road Bridge with zoomed-in northern (middle) and southern (right) sections.**

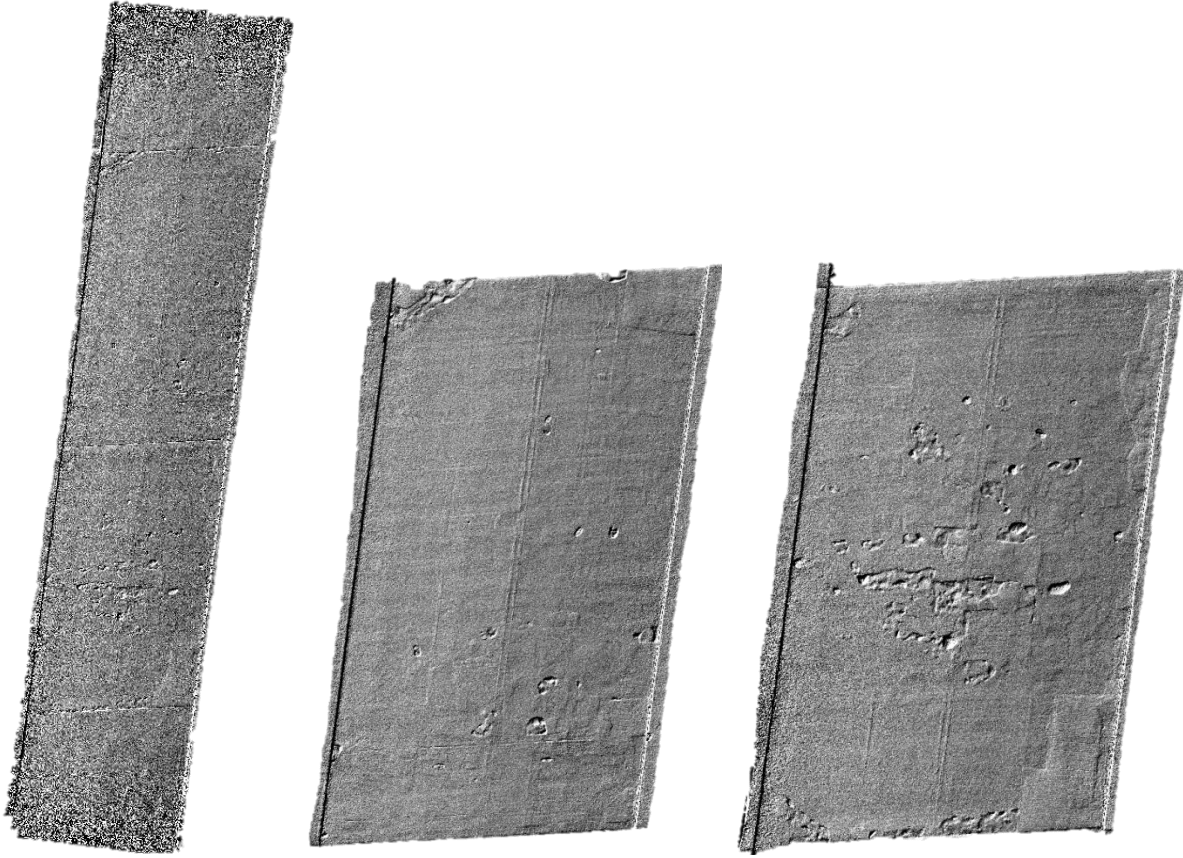


**Figure 4.1.1 G: Full bridge length (left) hillshade image of Stark Road Bridge with zoomed-in northern (middle) and southern (right) sections.**

The Tau2 plus ThermalCapture camera was mounted on the UAV, pointing in a nadir (vertical downward) direction, and flown over the bridge deck at an elevation of ~ 10 meters (33 feet) above the bridge level. This produced images with a ground pixel sizes between 1.3 and 1.4 centimeter (1/2 inch), and a total area coverage per image of ~ 3.3 x 4.7 meter (11 feetx 15 feet). The UAV flew back and forth at that elevation, along the orientation of the bridge, several times in an attempt to acquire a fully overlapping thermal imagery set of the bridge deck. Images in the native ThermalCapture 14 bit binary format were converted to standard 16 bit TIFF (tagged image file format) images and stored for further processing.

The high resolution and georeferenced orthophotography was used as the base layer to georeference the individual thermal image frames, captured by the Tau2 camera during the UAV flight. Georeferencing of the thermal images was done in ArcGIS, using reflective duct tape marks located on the bridge deck for that purpose. This enabled the thermal data to be laid directly on top of the optical bridge photos, enhancing image interpretation and usefulness of the data. The reflective tape marks are easily distinguishable in both the visible and the thermal images, and therefore can be used as tie-points between both datasets. Other distinctive and

naturally occurring features that could be identified in both datasets were used in addition as tie-points for the georeferencing process.

Figure 4.1.1 H shows the coverage of thermal imagery for both sites (bridges, at Merriman and Stark roads), overlaid on the visible orthophoto mosaic. Although the majority of the bridge is covered, due to a lack of real-time first-person-view for UAV operation of thermal image capture, led to parts of the bridge deck not being covered by the thermal imagery. The thermal imagery shows the complex and patchy structure of the bridge deck surface, caused in part by the many patches of repaired pavement and by pot holes and other surface discontinuities. Differences in patching material are reflected as differences in radiance values at the sensor, and although some may correspond to actual differences in temperature (some materials will absorb more radiation and heat up more by the solar radiation), some of the differences are likely to be mainly due to differences in the surface emissivity (e.g. Jensen, 2007). This complexity provides a challenging testing ground for the delamination classification methods, as will be explored in the next section.

In addition to the remotely sensed data collection at the field sites, a series of seven hammer soundings were also performed over delamination areas at the Stark Rd bridge deck (see Figure 4.1.1 I).

Potential delamination sites were first spotted using the handheld FLIR<sup>®</sup> SC 640 thermal camera, and were later tested with a hammer to confirm the presence of delaminations. The approximate extent of the delaminations was directly marked on the concrete. Other than the abnormally high thermal signals and the hollow sound produced by the hammer soundings, the seven areas did not show any visible signs of delamination, and would otherwise remained unnoticed (Figure 4.1.1 I). Of the seven areas with delaminations confirmed with the hammer soundings, six were covered by thermal imagery acquired from the UAV platform. The georeferencing process was further refined for thermal images covering these areas, as these images were selected for further and more in depth analysis, described in detail in the following section.

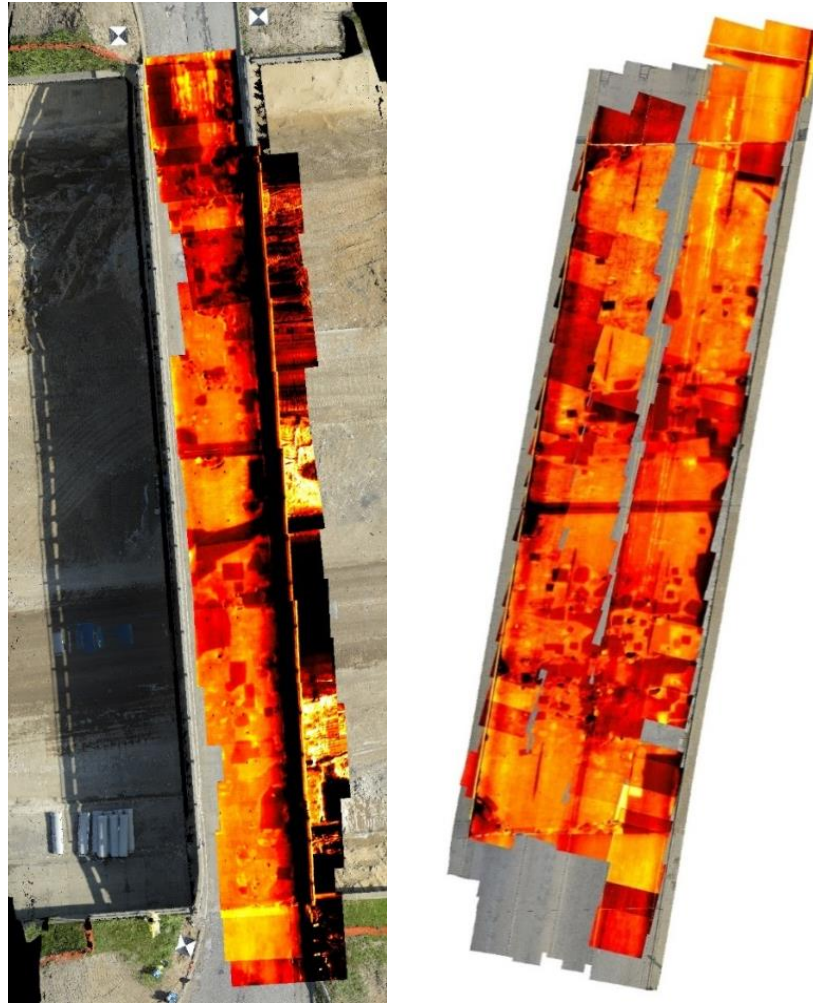


**Figure 4.1.1 H: Georeferenced thermal imagery acquired through the Tau2 and ThermalCapture camera system mounted on a UAV, overlaid on high resolution orthophotos, also acquired from the same UAV platform for Merriman East U-turn (left) and Stark Road (right).**

Figure 4.1.1 J shows the GPS position (red line) of the UAV over the Merriman East U-turn bridge. As the image shows, the GPS position is a good estimate of the UAV position. Using these data, we processed a 3-D point cloud by our algorithm described in Section 3.2.4. Figure 4.1.1 K and Figure 4.1.1 L show the processed 3-D LIDAR point cloud produced of the Merriman East bridge. As these images show, the 3-D point cloud is a very high-quality representation of the bridge, able to show the guard rail and curb, the surrounding embankments, and equipment on the ground under the bridge.

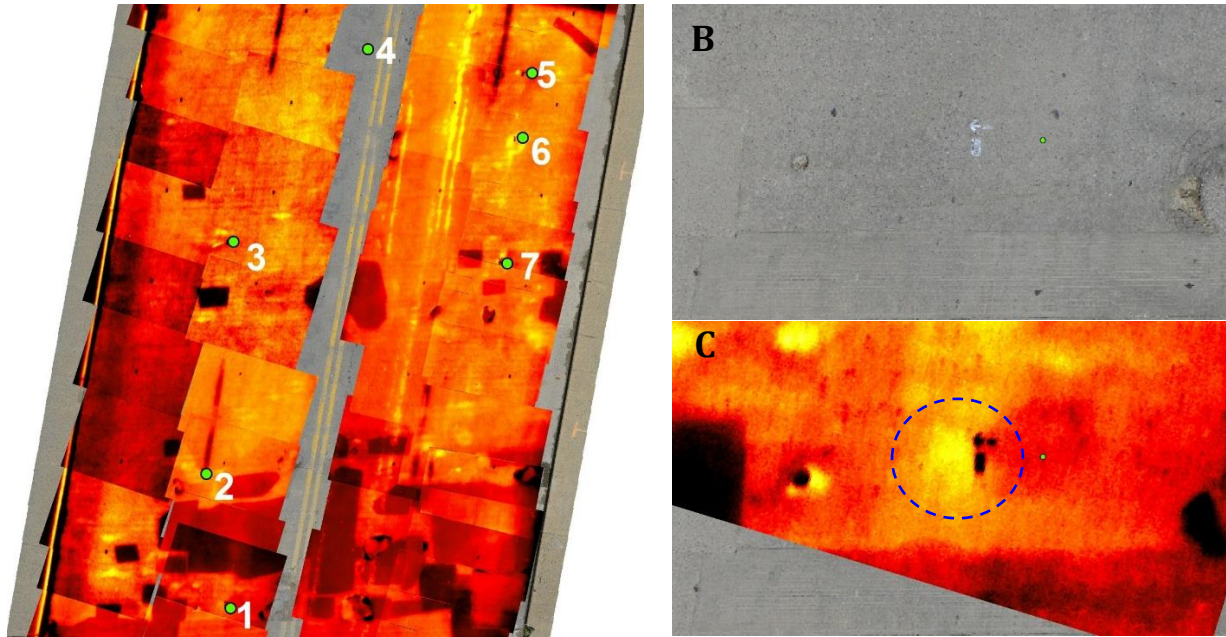


Figure 4.1.1 I: Delamination areas that were confirmed in the field through hammer sounding tests. A View of the delamination locations (green dots) with their respective number labeled in white. B and C show a close-up view of delamination area 1, in the visible and thermal bands, respectively. Notice the absence of any noticeable signs of the delamination in the visible band (B), in contrast to the clearly visible area of higher temperature shown in the thermal band (C), and indicated by the blue circle.

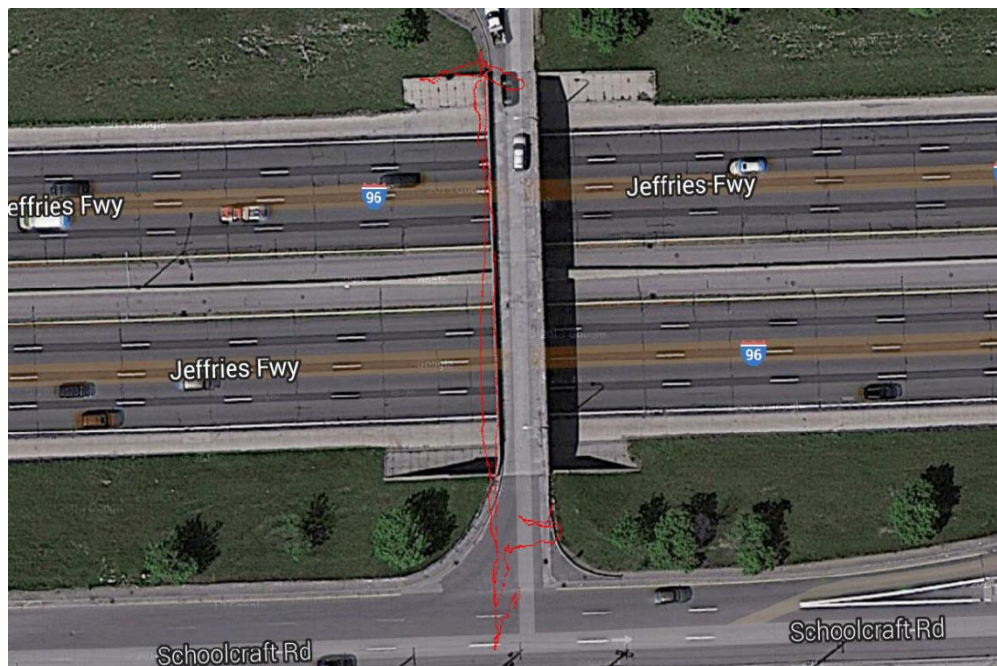
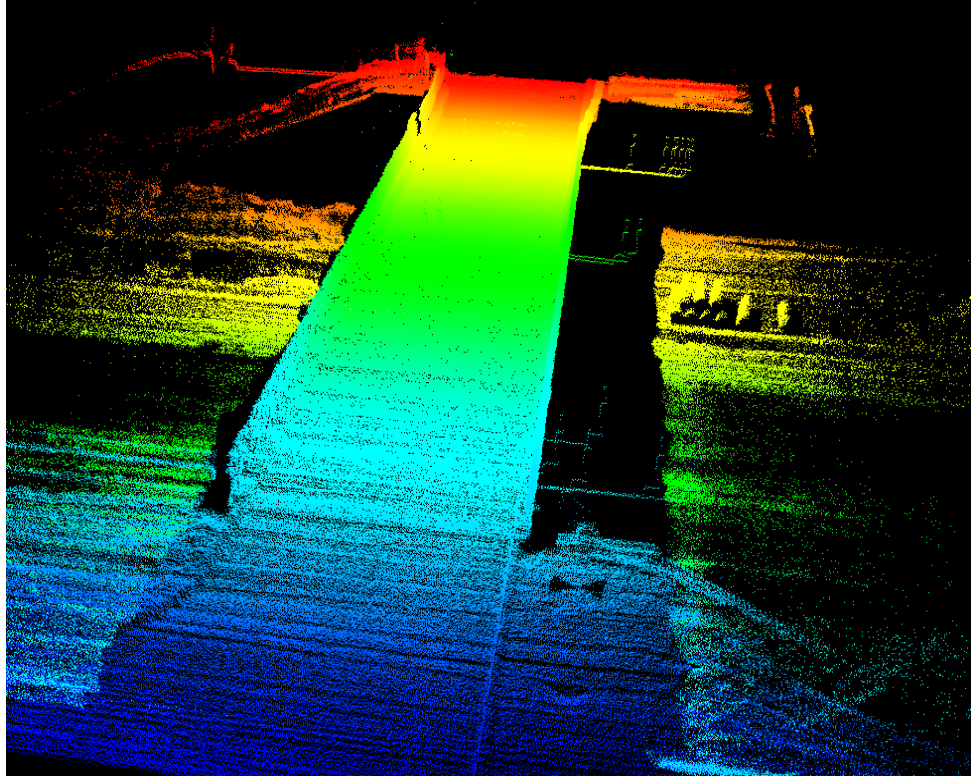
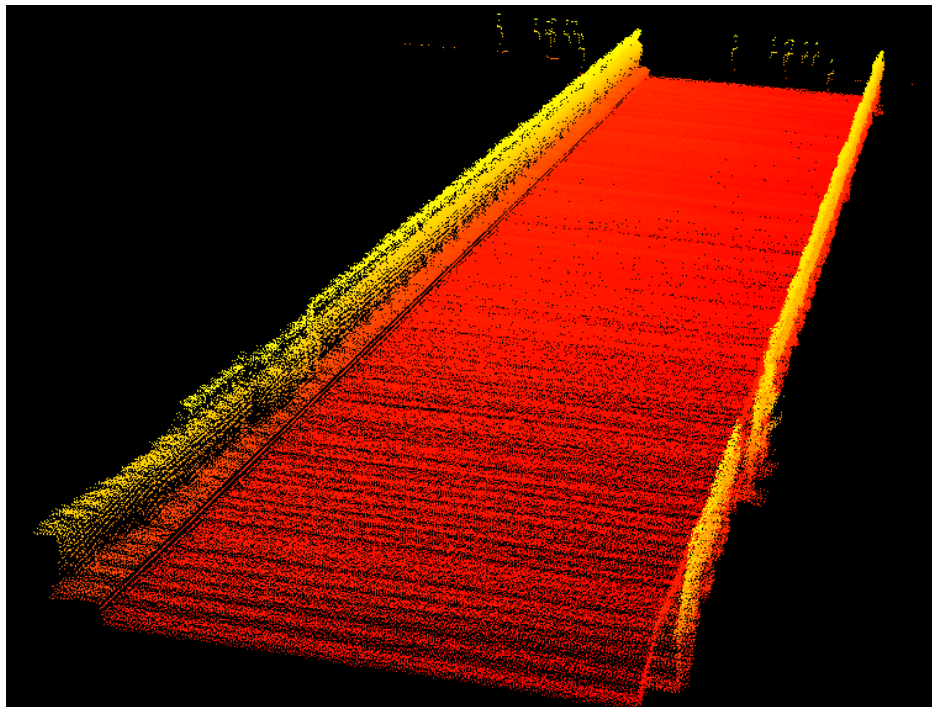


Figure 4.1.1 J: GPS tracking (red line) superimposed on Google Maps satellite image.



**Figure 4.1.1 K: 3-D LIDAR point cloud results of Merriman Rd. Bridge after using Michigan Tech LiDAR processing algorithm.**



**Figure 4.1.1 L: 3-D LiDAR point cloud of Merriman East U-turn bridge deck.**

#### 4.1.2 Performance evaluation of delamination mapping methods applied to test sites

The discussion in Section 3.2.6 on the delamination mapping and area quantification methods can be extended to the cases studied at the test sites on Merriman East and Stark Rds. The added complexity of the bridge deck surface, with a wide range of temperature and emissivity variations and combinations, presents a realistic challenge for any delamination mapping algorithm based on thermal remote sensing. Ideally we would test the performance of the thermal remote sensing method by comparing it to another independent delamination mapping method (e.g. hammer sounding or chain dragging). The extent of our hammer soundings is limited to only a few sites, preventing us to do a full quantitative evaluation of classification algorithm similar to what was done with the lab data. However we can still compare the performance of automatic mapping and classification algorithms described in the previous section, with the visual inspection method. Moreover, we can calibrate the visual observation method with the delamination identification done through hammer soundings.

Taking the areas mapped with the visual inspection methods as our reference, we can test how well the automated method (sliding window with local percentile threshold) reproduces what we generated by hand. ROC curves and related parameters were calculated for the six test areas, resulting in very similar classifications (see Table 4.1.2 A and Figure 4.1.2 A). The areas for these tests were chosen because of the available hammer soundings, but they are relatively simple, and this may explain in part the very good correlation between both methods.

**Table 4.1.2 A: ROC curve parameters for the test site delamination points. AUC is the area under the ROC curve. FPR50, TPR50 and Accu50 are the false positive rate, true positive rate, and overall accuracy at a threshold of 50th percentile. FPR90, TPR90 and Accu90 are the false positive rate, true positive rate, and overall accuracy at a threshold of 90th percentile. Note that these ROC curves only compare the local percentile threshold with visual inspection methods, the latter being used as the “true” reference.**

Point	AUC	FPR <sub>50</sub>	TPR <sub>50</sub>	Acc <sub>50</sub>	FPR <sub>90</sub>	TPR <sub>90</sub>	Acc <sub>90</sub>
1	0.97	0.39	0.99	0.62	0.03	0.79	0.97
2	0.96	0.40	1.00	0.61	0.04	0.68	0.95
3	0.98	0.40	1.00	0.60	0.05	0.91	0.95
5	0.98	0.45	1.00	0.55	0.06	0.97	0.94
6	0.97	0.45	1.00	0.55	0.04	0.79	0.95
7	0.96	0.43	0.99	0.58	0.05	0.82	0.95

All the study cases presented so far have only dealt with thermal imagery as the input for the delamination classification and mapping, but as mentioned previously in this section, high resolution photography in the visible range is available in a spatially co-registered format for the same areas covered by the thermal imagery. The information contained in this visible imagery can be used for the classification process as well, besides its use for georeferencing.

ROC curve for test site delamination sites.

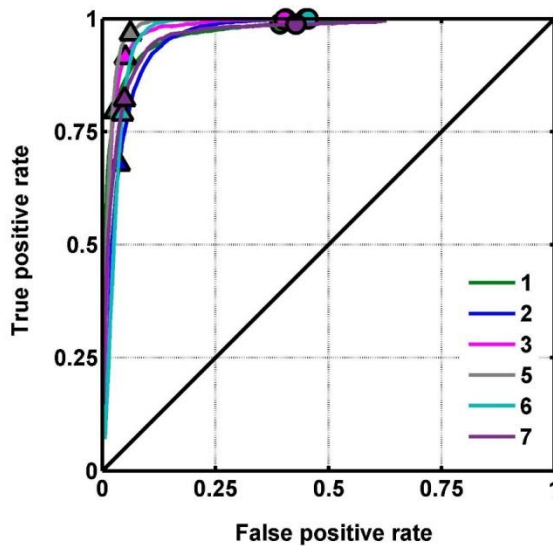


**Figure 4.1.2 A: ROC curve parameters for the test site delamination points. Circles and triangles in each plot mark the 50<sup>th</sup> and 90<sup>th</sup> percentile threshold points, for which the parameters are also given in Table 4.1.2 A. Curve colors represent the different testing points, as annotated in the figure legend.**

**Note that these ROC curves only compare the local percentile threshold with visual inspection methods, the latter being used as the “true” reference.**

Visible imagery was collected from the same UAV platform using the Nikon D800 camera. The sensor array on the camera responds to electromagnetic radiation in the visible (red through blue) part of the spectrum. Three different spectra are separated by a filtering system during image acquisition, resulting in separate pixel arrays for red, green and blue (RGB) color bands. Each band is recorded and stored in the camera files system in a single, eight bit, three band .jpg file. The RGB bands can be read separately from this file and used in multiband analysis. However, the materials commonly used in bridge deck surface , and roads in general, tend to be gray colored, ranging from very dark (almost black) asphalt, to very light (almost white) concrete. This color range is influenced by the ambient lighting and camera aperture conditions at the time of the data acquisition, but tends to be close to the gray tones of the surface material. The tendency to record the gray colors of the bridge deck surface is reflected as a high correlation of the RGB color values across the three bands for each pixel position, varying mainly in the recorded intensity of the luminosity, from values near zero representing darker hues (closer to black), to values near saturation (255 counts in the eight bit digital image), representing the lighter and brighter tones (closer to white). This high correlation of the RGB bands can be appreciated in the value distribution plots shown in Figure 4.1.2 B.

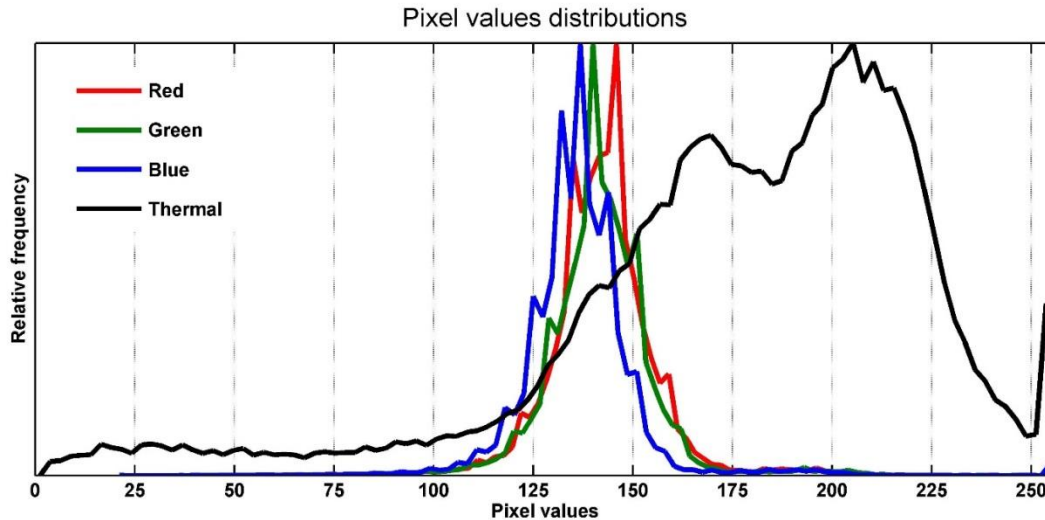


**Figure 4.1.2 B: Distribution of pixel values for an eight bit multiband image of the bridge deck surface. Visible bands (red, green, and blue) are all grouped in a relatively narrow and coinciding band, corresponding to gray tones, while the thermal band values are extended over a broader and not very correlated range.**

From the perspective of the multispectral analysis, the high correlation between the RGB bands implies a high redundancy of the data, such that each additional band provides little extra information. Standard multiband analysis, like principal component analysis (e.g. Jensen, 2007) would therefore benefit little from those extra bands. From a practical perspective only one of the visible bands could be used, discarding the other two, or the three bands could be combined (e.g. via a pixel-by-pixel averaging) into a single merged band. This last option is the one we implemented in our analysis, leaving us with two usable bands, the thermal IR and the combined visible (averaged RGB) bands.

Delaminations underneath the concrete surface usually do not produce visible signs at the surface. For that reason, the visible band will be of little help in trying to detect actual delaminations; instead, the value of the information contained in the visual band is in minimizing false positives. False positives in our case correspond to pixels that are classified under the category of “delamination”, when in reality they are not. In a thresholding algorithm method like the one we use, the classification of a pixel in the delamination category happens when the pixel is above some level of radiance with respect to its neighbors, as explained in the previous section. However, the assumption behind this criterion is that those higher radiance areas correspond to hotter regions on the concrete surface, caused by the presence of sub-surface delaminations (as also explained in the previous section). In reality there may be other reasons for pixels on the surface to show higher radiances than the surrounding background.

Differences in the surface emissivity due to changes in the material (e.g. patches of different concrete or even asphalt) can lead to large changes in the recorded radiance, which translate in

changes in the apparent brightness temperature (calculated assuming a constant emissivity). The changes in apparent brightness temperature can be caused by a change in surface emissivity (without an actual change in the surface kinetic temperature), a change in the temperature associated to the change in surface emissivity (because the surface will absorb more of the incident radiation and heat up), or in general, because of a combination of both.

In either case, this effect can mislead the algorithm into classifying areas where the surface material changes, into the delamination category, without real evidence for such a classification. However, such surface changes may easily be identified in the visible bands. In addition presence of foreign material (e.g. paint, shades, and leaves) on the bridge deck would produce thermal anomalies that are similar to delaminations (Del Grande 1996). This sets the rationale for using the visible band to control for false positives: areas that show up as hotter than the surrounding background are first checked to see if they are significantly different to the background also in the visible, e.g. areas with a different surface appearance in the visible band.

If an area shows up as a thermal anomaly, but not as significantly different in the visible band, it is classified as a delamination; as there is no evidence for surface changes that could explain the apparent higher temperature. If an area shows up as a thermal anomaly, but the same area shows up as significantly different than the surrounding background in the visible band, it is not classified as a delamination; as the change in apparent surface temperature is likely caused by the change in the surface characteristics. Figure 4.1.2 C shows the application of this algorithm to an area on the Stark Road test site, in this case changes in the surface material are the likely cause for what appears as a hot anomaly area in the thermal band, and could otherwise be mistaken for a delamination area.

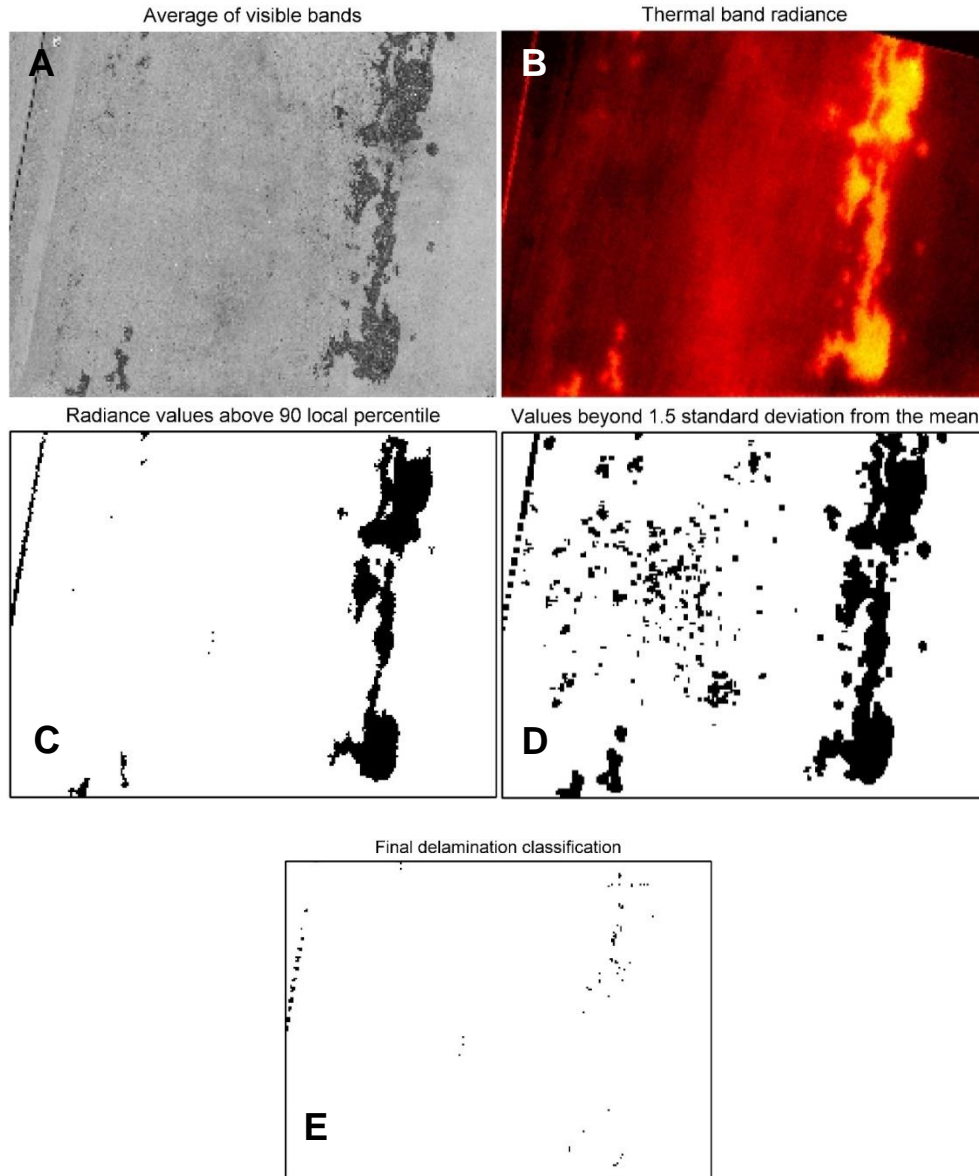
Finally, after the application of any or a combination of the methods described in the last two sections, it is possible to classify and map all the delamination areas, within certain margins of error. Knowing the spatial characteristics of the images, particularly the ground pixel size, the calculation of the total delamination areas becomes straightforward. Figure 4.1.2 D shows the application of such methods to one of the field test sites, the Stark Road Bridge. The total area of delaminations mapped through this method is 14.3 square meters (151 square feet) out of a total area covered by thermal imagery of 967.9 square meters (10,420 square feet) acquired over the bridge, resulting in a 1.5 percent of delamination area.

Figure 4.1.2 B was generated applying also some additional post-processing techniques (e.g. low pass, adjacency connectedness, and minimum area filtering) that are not described in detail in this report. This highlights the preliminary nature of our results and the need for more research to test more extensively and refine the methods that we presented here. Exhaustive delamination probing and testing through other methods in a real field setting are necessary to

further validate our techniques. With the exception of one post-processing technique (minimum area filtering) that was used in generating the results shown in Figure 4.1.2 D, all the methods explored and applied in project are “pixel based” and have the disadvantage of only marginally taking into account the spatial context (e.g. shape and size) of the mapped delaminations in the classification process. Methods based on feature recognition that use such a spatially contextual information may produce better results.

Although visible and thermal IR bands were combined to control for false positives in the classification process, other ways to integrate the different bands are also possible, especially if this can be extended to other datasets. One such datasets is the DEM produced from the close range photogrammetry that was conducted as part of the project; the elevation information, or probably more usefully, a surface roughness metric derived from it could also be used to characterize the surface properties and help in the classification process, similarly to what was done with the visible bands.

Comparisons with other sensors (e.g. larger pixel array Tau2) and improvements in the UAV platform interface, e.g. including a real-time thermal video feed to provide a first person view of the thermal sensor imagery as it’s being captured, would also improve the navigation and in that way the coverage of images over the target, minimizing data gaps. Integrating GPS locations with the sensor would also simplify the data processing. These ideas are proposed for a follow up phase to this project.



**Figure 4.1.2 C: Combination of thermal (A) and visible (B) bands to control for false positives in the delamination classification and mapping process. Threshold classification of high temperature areas produces the map in C, but from inspecting the visible image (B) it becomes apparent that such areas show up as “hot” probably due to changes in the surface material. A map of pixels outside with values beyond 1.5 standard deviations from the local mean for the visible band is produced in D, and is used to control for the false positives: i. e. only pixels that show radiance values above the local background and do not deviate much from the local mean in the visible band are classified as delamination pixels in E. This virtually eliminates all the pixels that originally were classified as delamination pixels based only on the thermal band threshold information.**

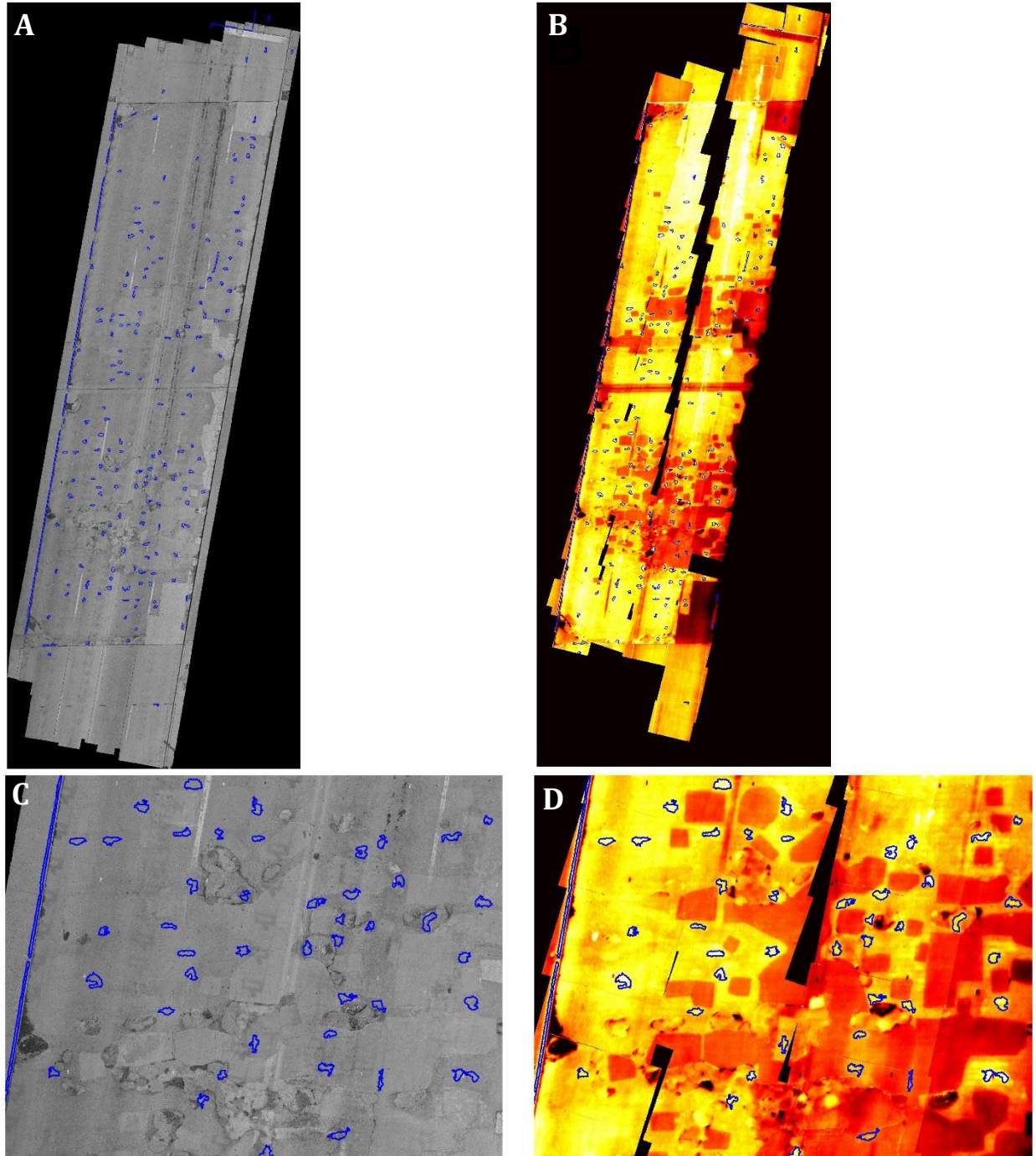


**Figure 4.1.2 D: Overview of the entire bridge-deck in the visible (A) and thermal (B) bands, with delamination areas shown by the blue polygons. A close-up view of a section of the deck is also presented in C (visible) and D (thermal), with delamination areas also shown by the blue polygons.**

## **4.2 Confined Space - Pump Stations and Culverts**

Field demonstrations of pump stations were conducted in the Elm Street (Figure 4.2 A) and the River Rouge Pump (Figure 4.2 B) Stations along Interstate-696 on April 25, 2014. The main

objective was to fly a micro UAV into the lower section of a pump station through the access hatch and then fly around and collect imagery of the condition. For these flights the Heli-Max 1Si and the Walkera QR 100S were selected. This decision was made after successful testing in the MTRI lab that they are capable of flying in confined spaces as well as through doorways and spaces where there is only a three feet of clearance. The Phantom 1 that was used in the initial testing is too large to safely fit through the hatch openings of pump stations especially with its tendency to be pulled into the sides.



**Figure 4.2 A: Overview of the Elm Street Pump Station along I-696 in Roseville, MI.**

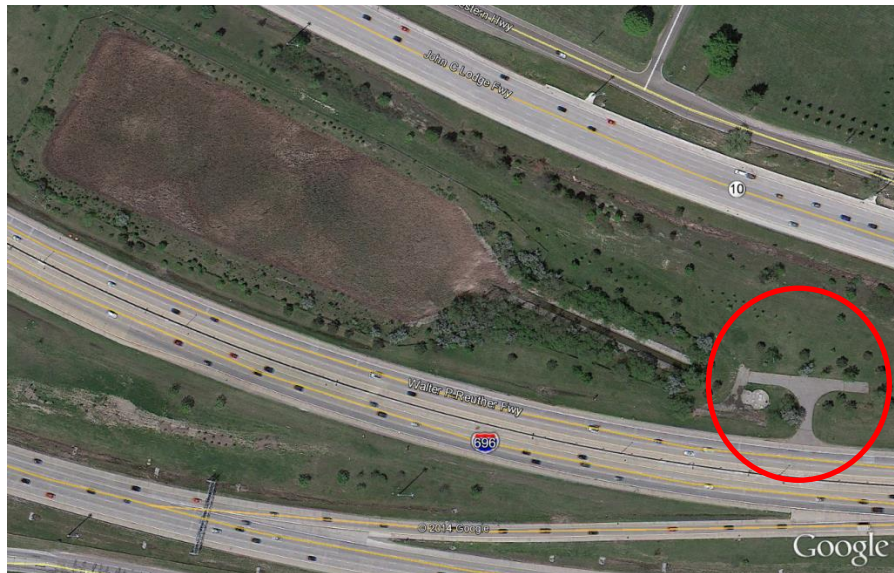


**Figure 4.2 B: Overview of the River Rouge Pump Station in Southfield, MI.**

The first attempt through the Elm Street pump station hatch was unsuccessful. The Walkera QR 100S went through the hatch slowly and it was caught in vortices that pull it into the I-Beam just under the hatch (Figure 4.2 C). Upon trying to fly off the beam, it again was pulled into the

wall and fell into the pool at the bottom of the station (Figure 4.2 D). This first attempt through the hatch of the pump station showed that the unpredictable air currents and turbulence from the UAV would be an issue when trying to enter slowly through the hatch, and served as a valuable testing lesson. It is noteworthy that losing a \$200 micro-UAV is still worth the imagery that it could send to assess whether it is safe to enter the confined space.



**Figure 4.2 C: The opening of at the Elm Street Pump Station that the micro UAVs flew through for the demonstrations. The I beam that caused an issue with the first attempt is on the lower left of the opening. The opening is approximately 4 feet x 3 feet.**



**Figure 4.2 D: The Walkera UAV having just lost control after making contact with the wall of the pump station.**

The next attempt was made with the Heli-Max 1Si. This attempt was made with the UAV quickly dropping through the opening so that there was not enough time for the turbulence to reach the UAV as it passed through. Figure 4.2 E shows the Heli-Max about to make a successful pass through the opening and Figure 4.2 F shows it right after passing through.



**Figure 4.2 E: The Heli-Max 1Si about to pass through the opening into the lower section of the pump station.**



**Figure 4.2 F: The Heli-Max 1Si right after passing through the opening into the lower section of the pump station.**

Video was collected in the lower section of the pump station after the UAV made it into the lower section. Since the Heli-Max does not have the capability to transmit video back to the operator, these flights were conducted within line of sight. As seen in Figure 4.2 G, high quality imagery was able to be collected of the pump station.



**Figure 4.2 G: An extracted frame from a micro UAV flight into the lower section of a pump station.**

The River Rouge site provided an additional challenge for flying. It did not have a large opening similar to the Elm Street Pump Station which would make it difficult to see the UAV once it's in the lower level. The largest opening into the lower section was for the ladder but the cage around it prevented a flight from starting at the main level. For this station the flights were launched from a stand that was used to change the light (Figure 4.2 H).

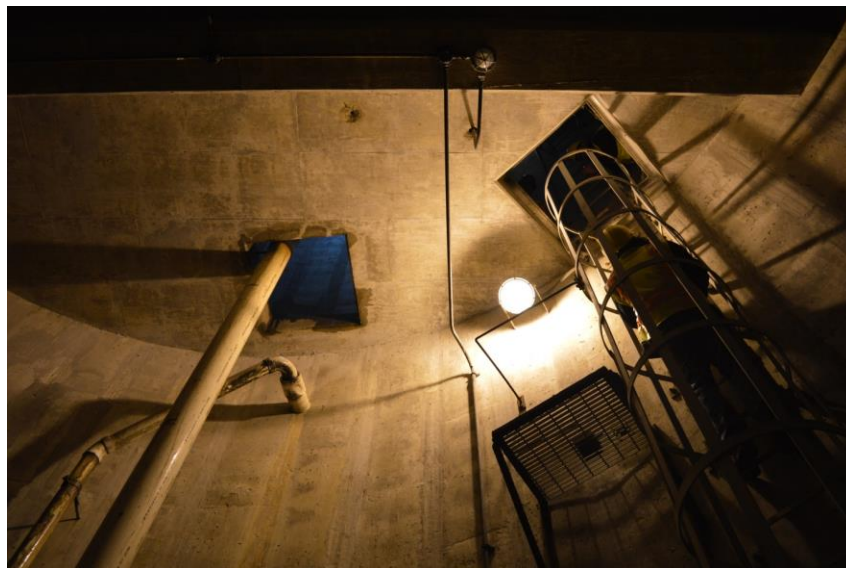


**Figure 4.2 H: Looking up at the ladder and the opening of the River Rouge Pump Station from the lower level.**

Several flights were made in this pump station using the stand (Figure 4.2 I). An earlier version of the Walkera UAV was also made ready to fly at this pump station since losing the QR 100S in

the Elm Street Pump Station (Figure 4.2 J). The Walkera was able to transmit video of the inspection back to a cell phone while in the pump station (Figure 4.2 K).

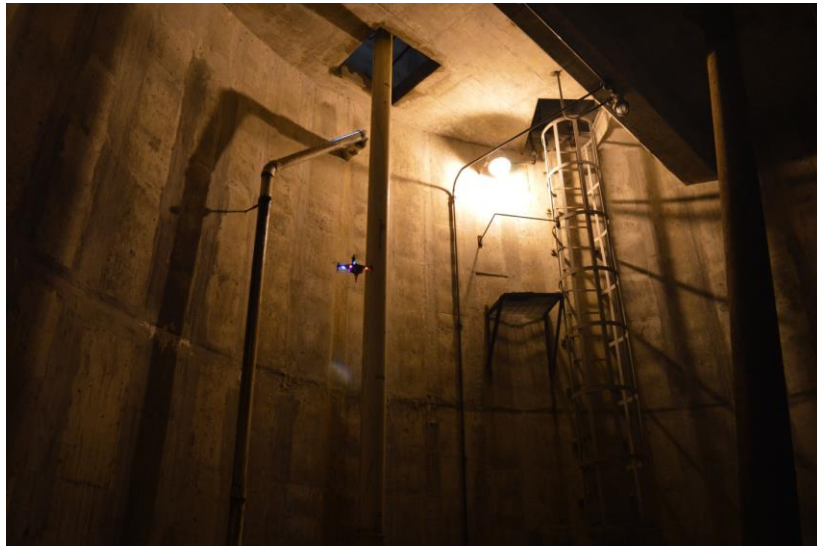


**Figure 4.2 I: Heli-Max 1Si flying and collecting video of the River Rouge Pump Station.**



**Figure 4.2 J: The Walkera QR 100 flying in the River Rouge Pump Station.**



**Figure 4.2 K: Video being streamed back to a cell phone as the Walkera 100 is inspecting the River Rouge Pump Station.**

### **4.3 Traffic Monitoring**

The blimp traffic monitoring system had its field demonstration at the ITS World Congress in Detroit September 8-11, 2014 where it was deployed on Belle Isle for four days (Figure 4.3 A). The camera transmitted imagery via 4G from the island back to a mockup of a Traffic Operation Center at Cobo Hall in downtown Detroit. The blimp was flown continuously during the day and was stored still inflated in the rental truck at night.

Operationally, only a small top-up of helium was needed in the morning, after the blimp was removed from the back of the truck where it was stored for the night. The weather was generally good, although the island was shut down one afternoon as a result of an oncoming storm. Wind was generally not a problem and the blimp flew well over the four day event.



**Figure 4.3 A: The MTRI blimp at the ITS World Congress site on Belle Isle.**

The blimp was flown over the mock incident on Belle Isle Tuesday afternoon (Figure 4.3 B). It was on station during the entire event with the exception of when the medevac helicopter arrived and departed. Although the gimbal was not functioning and the camera was not always pointed where the action was, it gave a good sense of the kind of images that can be obtained from an aerostat.



**Figure 4.3 B. Screenshots from the MTRI blimp video feed of the emergency response mock incident. The blimp was approximately 100 feet in the air when these shots were captured.**

#### **4.4 ITS World Congress**

The project team provided a significant presence sharing and promoting MDOT as being in the forefront of advanced research ideas at the 21<sup>st</sup> World Congress on Intelligent Transportation Systems (also known as the ITS World Congress), held at Cobo Center in Detroit on September 7 through 11, 2014. Starting in May of 2013, MTRI team members regularly attended planning meetings organized by Michele Mueller of MDOT, at the request of Program Manager Steve Cook; nine meetings were attended in all.

The initial concept discussed with Program Manager (PM) Cook was to provide a demonstration of at least one technology in Cobo Hall to show how this UAV-focused project could help provide needed data for the ITS community. Over time, this concept grew into providing ten main demonstration, outreach, and interaction opportunities available through the ITS World Congress:

- 1) Provide a four-day outdoor series of demonstrations of UAV technologies at the Technology Showcase area on Belle, including the project's traffic monitoring blimp, the Bergen hexacopter used for collection of bridge condition data, and the small DJI Phantom 2 quadcopter used for tasks such as imaging the underside of bridges and transportation corridors.

- 2) Have a booth presence in the Technology Showcase preview area inside Cobo Hall to share project progress, and help direct people to see demonstrations at the outdoor Technology Showcase.
- 3) Fly indoors at Cobo Hall at the ITS Test Track to demonstrate the capabilities of the small quadcopter, including flying through a small section of culvert shared by the RCOC.
- 4) Participate in MDOT's TOC inside Cobo Hall, including providing a live feed of video from the traffic monitoring blimp being flown during Monday morning through Thursday morning out at Belle Isle, with the video being displayed on one of the two large video walls.
- 5) Give a 15-minute talk at the Cobo Hall TOC during one of the Spotlight Presentation slots on Wednesday, September 10<sup>th</sup>, on how UAVs can be used to meet transportation data needs as demonstrated through this MDOT research project.
- 6) Present at a Technical Sessions focused on "Innovations in Video and Aerial Sensing" (Session #32) with a paper and a talk entitled "Evaluating the Use of Unmanned Aerial Vehicles for Transportation Purposes: A Michigan Demonstration" on the Tuesday morning of September 9<sup>th</sup>.
- 7) Include a flight and imagery demonstration on how UAV-based imagery collection could provide useful data as part of the Mock Incident at Belle Isle during the Tuesday, September 9<sup>th</sup> Emergency Responder Day.
- 8) Share project capabilities that fit into the priorities of the MDOT Office of Aeronautics by providing a brief series of slides that could be shared as part of their display area in the Michigan Showcase.
- 9) Create an initial brief promotional video and longer 10-minute descriptive video sharing the project capabilities, with the promotional video available via Youtube in the week leading up to the conference (and shared via Twitter) and the longer descriptive video being shown at the Technology Showcase booth and as background for the C.Brooks Technology Showcase Spotlight Presentation. These were videos also shared through the project website that was approved and posted in the run-up to the ITS World Congress, at [http://www.mtri.org/mdot\\_uav.html](http://www.mtri.org/mdot_uav.html).
- 10) Post an article on the Michigan Tech News website describing the research project and how its progress would be shared through demonstrations and other outreach at the ITS World Congress (<http://www.mtu.edu/news/stories/2014/september/mtri-demos-uses-for-unmanned-aerial-vehicles-transportation.html>).

## 1 – Outdoor UAV demonstrations at Belle Isle

The hexacopter UAV, DJI Phantom 2 UAV, and the traffic monitoring blimp were all demonstrated during the outdoor part of the Technology Showcase at Belle Isle on Monday through Thursday, including during the Michigan ITS Festival on Tuesday, September 9<sup>th</sup> when many conferences attendees moved over to Belle Isle, helping with additional exposure. The project team had a Michigan Tech booth near the historic Casino Building where attendees could come ask questions, see the hardware on the ground, and view flight demonstrations and the blimp operations. Team members David Dean, Ben Hart, Rick Dobson, Chris Roussi, Colin Brooks, Nate Jessee, and Blaine Stormer helped at various times with the Belle Isle demonstrations. Figure 4.4 A shows the traffic monitoring blimp collecting data over Belle Isle. Figure 4.4 B shows a screenshot of the live video stream that was shared through the TOC and on-site tablets (this was close to live; the video stream experienced a 10-15 second delay using the USTREAM application that the team used to share the video). Over seven hours of recorded video from the blimp demonstration are available at the MTRI USTREAM site at <http://www.ustream.tv/channel/mtri>.



**Figure 4.4 A: The traffic monitoring blimp collecting near-live video data over Belle Isle during the ITS World Congress.**

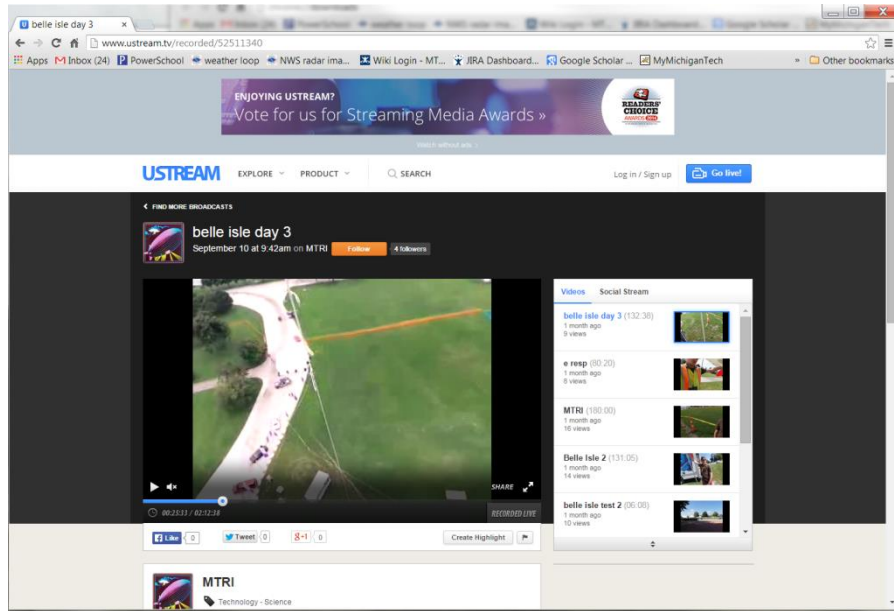


**Figure 4.4 B: A screenshot of the near-live video feed that was shared through one of the Traffic Operations Center video walls.**

Figure 4.4 C shows an example of the hexacopter UAV being demonstrated to several interested World Congress attendees. Rather than the limited 3-4 a day set of flights originally planned, the demonstration team expanded this concept to 10 or more short (3-5 minute) flights through the day to help more attendees understand the capabilities of the system. Technical team members were available throughout the demonstration day to answer questions, share handouts, and operate the equipment. A count of the number of people reached is hard to quantify, but groups of attendees came throughout the day, often in batches of two to 10, so at least several hundred attendees saw the demonstrations, possibly into the low thousands. A short, 36-second segment showing the hexacopter demonstration at Belle Isle also made the Fox 2 Detroit evening TV news.



**Figure 4.4 C: Belle Isle Technology showcase attendees viewing a demonstration of the Bergen hexacopter UAV.**

## **2 – Booth presence at the Technology Showcase**

A project handout (approved by MDOT) and a handout describing MTRI were available in the booth, as were UAV equipment when they were not in use. The project demonstration video made for the Spotlight Presentation was shown at times, and at other times, a slideshow with over 250 graphics and photos was shown to help attendees understand what was being accomplished through this research project. The booth was staffed for nearly all of the time the ITS World Congress exhibit floor was open, with attendees coming by regularly to ask questions. Information about the technologies and research project were shared, and attendees were encouraged to view the technology demonstrations out at Belle Isle and to see the video feed from the traffic monitoring blimp at the TOC. Figure 4.4 D shows team member Michelle Wienert sharing project information at the Michigan Tech Technology Showcase booth.



**Figure 4.4 D: Project team member Michelle Wienert sharing the UAV project information with World Congress attendees.**

### **3 – Indoor Cobo Hall flights at the ITS Test Track**

Two to four times a day, team member Rick Dobson flew a small quadcopter (either the DJI Phantom 2 or the Blackout Mini-H Quad) inside Cobo Hall over the indoor ITS Test Track demonstration area, including flights through the RCOC-provided section of culvert. This enabled UAV demonstrations to take place even when weather was inclement outside, to show an example of flying through a confined space (culvert), and to enable ITS Exhibit Hall attendees to get an example of UAV capabilities (see Figure 4.4 E).

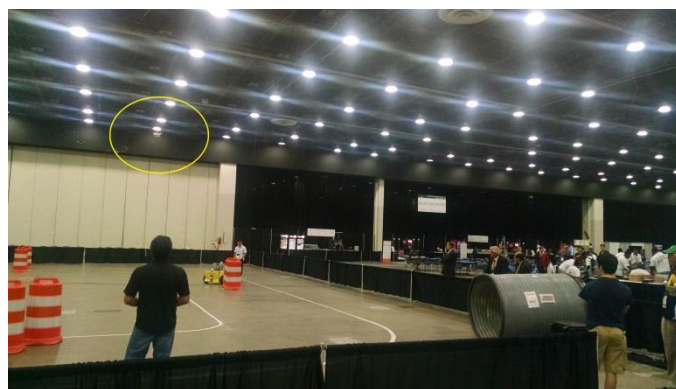


**Figure 4.4 E: A small DJI Phantom quadcopter (circled in yellow) being flown over the indoor ITS Test Track in the Cobo Exhibit Hall; onlookers are viewing the demonstration and the RCOC culvert piece can be seen on the lower right.**

#### 4 – Traffic Operations Center video wall participation

A major part of the project team's effort during the ITS World Congress was demonstrating how near-live video could be collected and transmitted to a traffic operations center using the project's traffic monitoring blimp. Tethered out at Belle at the Michigan Tech demonstration area, the blimp operated for most each demonstration day out at Belle Isle from late Monday morning through Thursday morning. Over seven hours of video were recorded and saved. Video was also streamed from the blimp during the Emergency Response Day Mock Incident. The blimp has a Samsung 4G digital camera slung underneath it, with the built-in Verizon 4G providing the capability to transmit the video over the cell phone network. This video was sent to the USTREAM web-based image streaming service using the USTREAM app that was installed on the Samsung 4G camera. With a small delay of 10-15 seconds, the USTREAM service then makes the video available for access via their web page; the Belle Isle videos were available at <http://www.ustream.tv/channel/mtri>. A free 30-day account was used for the ITS World Congress; plans start at \$99/month after the initial month. Other near-live video sharing web-based services are available and the project team is not trying to recommend USTREAM as the only or even the main solution for retransmitting blimp-based video. An implemented, operational service would be developed in concert with MDOT taking advantage of their technology capabilities wherever possible, such as their existing ground-based traffic camera video sharing technology.

Figures 4.4.F shows an example of the Belle Isle blimp-based video being shared on the south video wall at MDOT Traffic Operations Center area the ITS World Congress. As noted, this was display a near-live video feed for most of the ITS World Congress; when the blimp wasn't operating (such as the Wednesday afternoon when there was a thunderstorm), a recording of the video feed was displayed instead to demonstrate the concept. A team member, usually David Banach, was there the entire time the Exhibit Hall was open to help answer questions from interested attendees.



**Figure 4.4 F: The traffic monitoring blimp video is being displayed in the top left of the MDOT ITS World Congress TOC south video wall, enabling attendees to see the type of near real-time traffic information that can be shared through this system.**

## **5 – Spotlight Presentation**

Principal Investigator (PI) Colin Brooks gave a 15-minute talk as one of the Spotlight Presentations at the TOC. Included as part of this talk was a background video, created with MDOT input, that was displayed temporarily on the south video wall with video and still pictures from UAV-based data collections to help demonstrate the project’s concept, progress, and technical capabilities. This video was uploaded to Youtube and is available at <https://www.youtube.com/watch?v=dCgKplgnn6c>. Figure 4.4 G shows a screenshot of the Youtube video that was shared with the Spotlight Presentation attendees (at least 25 people saw the talk) (Figure 4.4 H).

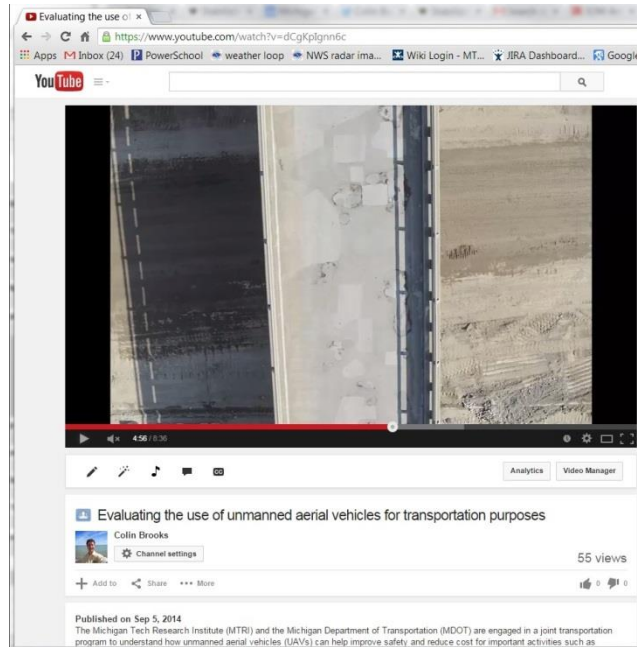


**Figure 4.4 G: A screenshot from the Youtube video that was used to help describe the MDOT UAV project to attendees during the Spotlight Presentation and at the Michigan Tech Technology Showcase booth.**



**Figure 4.4 H: PI Colin Brooks gave the Spotlight Presentation talk to ITS World Congress attendees.**

## **6 – Technical Session Presentation and Paper**

PM Cook requested that the project team submit a conference proceedings paper to the ITS World Congress, which was accepted and included as part of Technical Session 32 at the conference. PI Brooks gave his 20-minute talk, with approximately 30 people in the audience, as part of a four-person session which included another presentation on UAVs from a European

transportation perspective. The conference proceedings paper was written and accepted, and has the citation of:

Brooks, C., T. Oommen, R.J. Dobson, D. Dean, D. Banach, T. Oommen, T. Havens, T. Ahlborn, S. Cook, A. Clover. 2014. Evaluating the Use of Unmanned Aerial Vehicles for Transportation Purposes. Proceedings of the the 21<sup>st</sup> World Congress on Intelligent Transportation Systems, Detroit, MI. Paper No. 13608, 14 pgs.

The submitted and approved abstract for the talk read as follows: “This technical paper reviews advancements being made in applications of Unmanned Aerial Vehicles (UAV) for helping the Michigan Department of Transportation with its asset management condition assessment and inventory needs. Transportation departments are interested in leveraging technologies to achieve efficiencies in operations, maintenance, and asset management. Confined spaces, bridge surfaces, traffic, and roadways are being assessed with multiple sensors to understand what combination of inexpensive small UAVs and sensors can be practically deployed for transportation applications. Examples of collecting useful imagery with a small UAV in confined spaces and large UAV based deployments above bridge decks have demonstrated using thermal infrared, LiDAR, and three-dimensional optical sensors. Demonstrations are planned for the 21st World Congress on Intelligent Transportation Systems being held in Detroit, Michigan in September 2014.”

## **7 – Emergency Response Mock Incident Participation**

Angie Kremer of MDOT, with approval of PM Cook, asked for the Michigan Tech team to participate in the Emergency Responder Day Mock Incident. The project team’s role was to work closely with the MSP, MDOT, and other participants to show how UAV-based imaging could provide useful data on a practical basis during an emergency response incident representative of where lives were at risk and information was needed as quickly possible that could be collected safely. Figure 4.4 I shows an overhead image of the mock incident freight vehicle taken from the Bergen hexacopter; this information was made available to the incident command center as soon as the hexacopter landed. The traffic monitoring blimp was rapidly moved over to the incident area to make the video feed available as well. Team members Rick Dobson and Ben Hart were complimented by Sgt. Shackelford of the Bloomfield Township police for their rapid help and for working well within the flow of the incident. Figure 4.4 J shows R.Dobson and B.Hart just having deployed the hexacopter for collecting overhead imagery after having arrived in an Auburn, MI police vehicle also carrying the hexacopter.



**Figure 4.4 I: The hexacopter UAV was able to take this photo of the Mock Incident and then share it immediately after completion of the flight.**



**Figure 4.4 J: The hexacopter starting to collect imagery during the Mock Incident.**

## **8 – Office of Aeronautics shared information**

Approximately two months before the ITS World Congress, Matt Brinker from the MDOT Office of Aeronautics asked for a representative of project images that they could include in their display that was part of the Michigan Showcase area. Images and videos showing blimp-based traffic monitoring, bridge condition evaluation, and pump state inspections were shared and included in Mr. Brinker’s showcase display. Figure 4.4 K shows an example of one of the photos that was shared for display.



**Figure 4.4 K: An example of one of the images shared with Matt Brinker for display in the MDOT Aeronautics area; this one shows an overhead image of bridge deck patching and spalls collected with the hexacopter UAV.**

## **9 – Project demonstration videos**

As mentioned, two videos were prepared for helping share project information in the run up and during the ITS World Congress, with team member David Banach developing these. The short video was requested by Michele Mueller to give a preview of what would be demonstrated during the ITS World Congress, and was shared through the World Congress website in advance of the actual conference. It is available at <https://www.youtube.com/watch?v=-xnTP4ZA1Nk>. A longer video was made to give a larger description of the project and was shown during the Spotlight Presentation and at the Michigan Tech booth so that attendees could always be viewing example project results. It is available at <https://www.youtube.com/watch?v=dCgKplggn6c>. PM Cook reviewed both videos and provided input, especially on wording for the project. The longer video was well received by attendees who were able to get a short overview of the project by viewing the video.

## **10 – Michigan Tech News article**

As part of the lead-up to the World Congress, Michigan Tech’s Director of News and Media Relations Jennifer Donovan prepared an article for the Michigan Tech News website that was reviewed by MDOT and promoted by Michigan Tech starting on its September 5<sup>th</sup>, 2014 posting. It included a graphical review of the project, and information about the UAVs and the data that they were capable of collecting to meet transportation asset management and condition assessment needs. Figure 4.4 L shows a screenshot of the web news article which is available at <http://www.mtu.edu/news/stories/2014/september/mtri-demos-uses-for-unmanned-aerial-vehicles-transportation.html>.

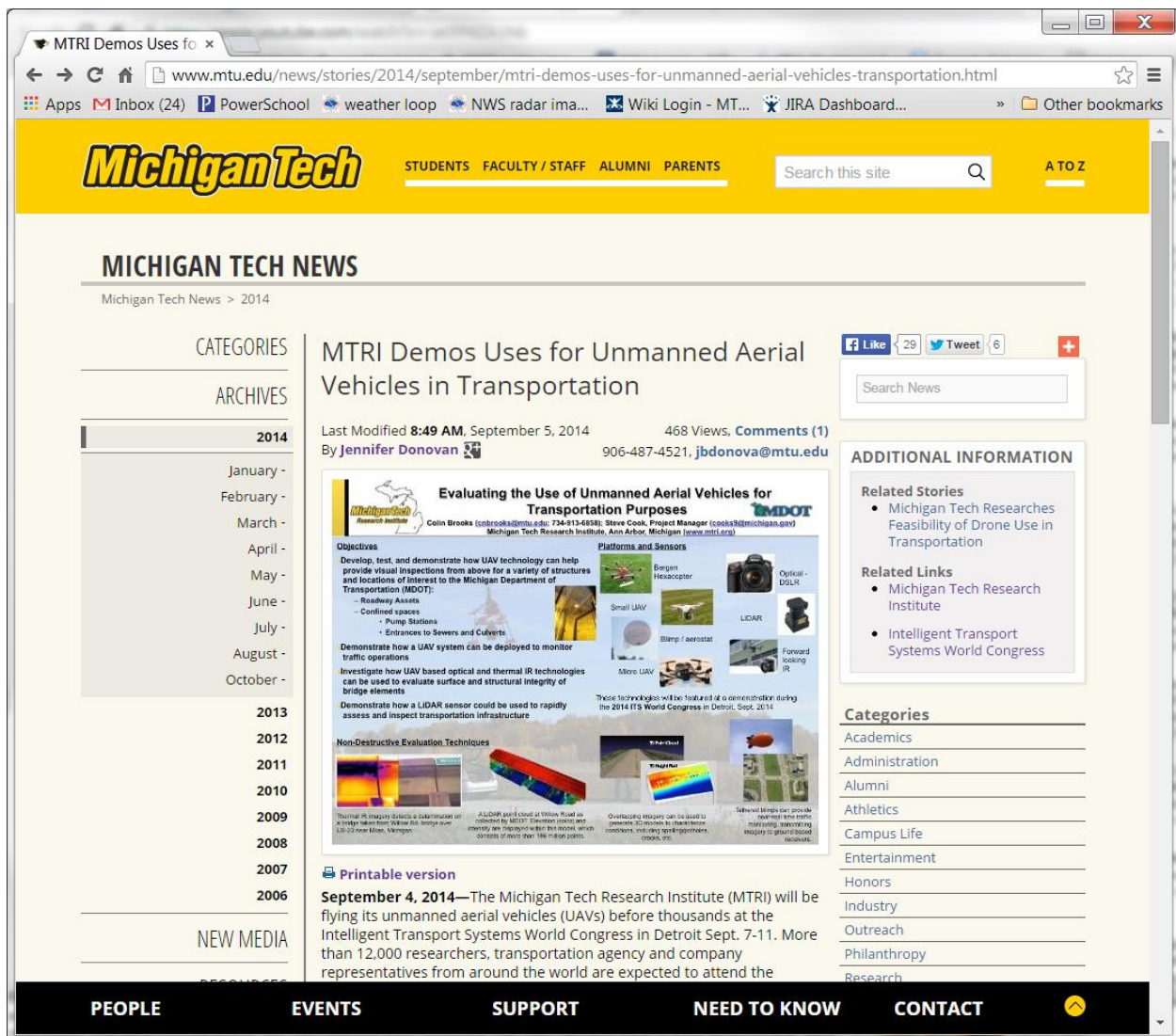


Figure 4.4 L: A screenshot of the Michigan Tech News article released in advance of the ITS World Congress to help promote the project team’s participation and MDOT’s backing of advanced research.

## 5. Procedures

### 5.1 Bridge Deck Condition Multi-source Data Evaluation

This section serves an example of the types of procedures use to successfully collect needed data using UAVs with appropriate sensors. As the I-96 Fix bridge flights were the locations that included the widest set of platforms and sensors, we have focused on those data collection as our data processing and data merging procedures example.

Multiple sources of data such as optical photogrammetry and thermal can be brought together in a GIS to gain a more complete perspective of the overall condition of a bridge deck. When results are combined, the inspector is able to visualize surface and subsurface distresses. Both

optical and thermal data can be collected from a UAV and referenced using geotagged photos using a GPS or through markers placed on the deck itself.

The collection of optical and thermal data is similar in that both cameras are mounted to a UAV and they collect imagery as it is flown over the bridge deck. There are two differences in imagery collection between the Nikon D800 used for the optical collects and the thermal camera. The first is that the Nikon D800 is capable of a higher frame rate than the thermal camera. The higher frame rate would allow for the UAV to pass over the bridge deck faster than with the thermal camera. The second is that the Nikon D800 had a 50 millimeter prime lens which has a wider field of view than the thermal camera. This difference would allow the D800 to collect two lanes per pass from an altitude of 100 feet while the thermal camera would collect just over one lane from the same altitude. For collection and referencing purposes the Nikon D800 had a GPS attached which would geotag the photos as they were taken.

### Generating 3D models

All of the optical imagery was processed in Agisoft Photoscan Pro. This is a commercially available software that uses structure from motion to generate 3D point clouds from stereo imagery pairs (costing approximately \$3500). This software is able to calculate the relative positions of the camera as the image was captured. For this, there needs to be at least a 60 percent overlap in the imagery.

The first step in the Agisoft process is to bring the photos into the project. Figure 5.1 A shows an example of images that have been brought in. The estimated relative positions of the photos, based on the geotag information, are displayed.

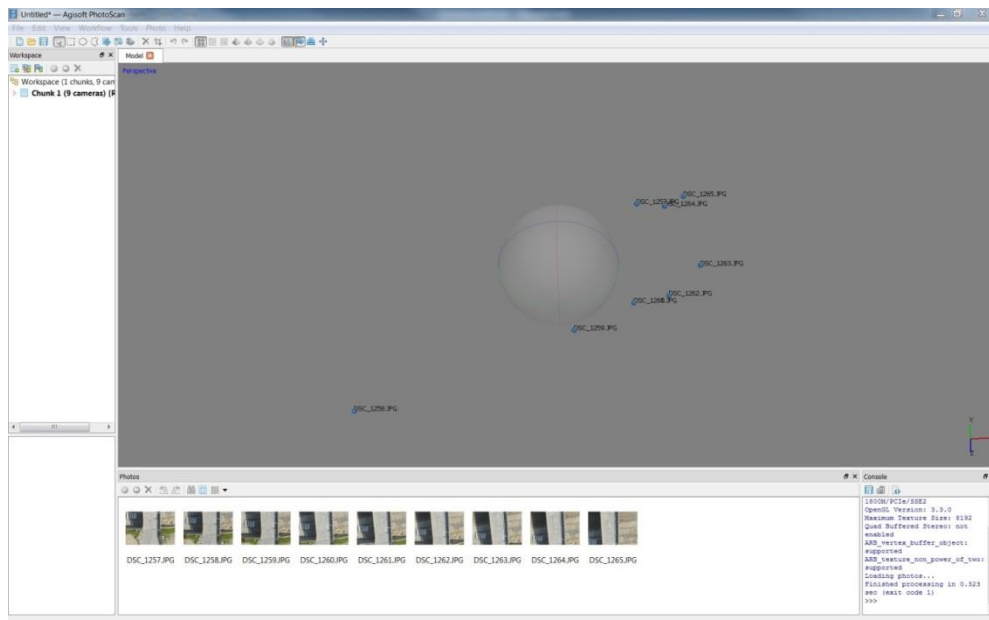


**Figure 5.1 A: Photos added to an AgiSoft project for processing.**

In the next step the user selects the "Align Photos" command. This command uses the structure from motion algorithm to calculate the relative positions of where each of the photos were taken and creates a sparse point cloud of the scene being modeled (Figure 5.1 B). The photo alignment is done automatically and does not require any user input.

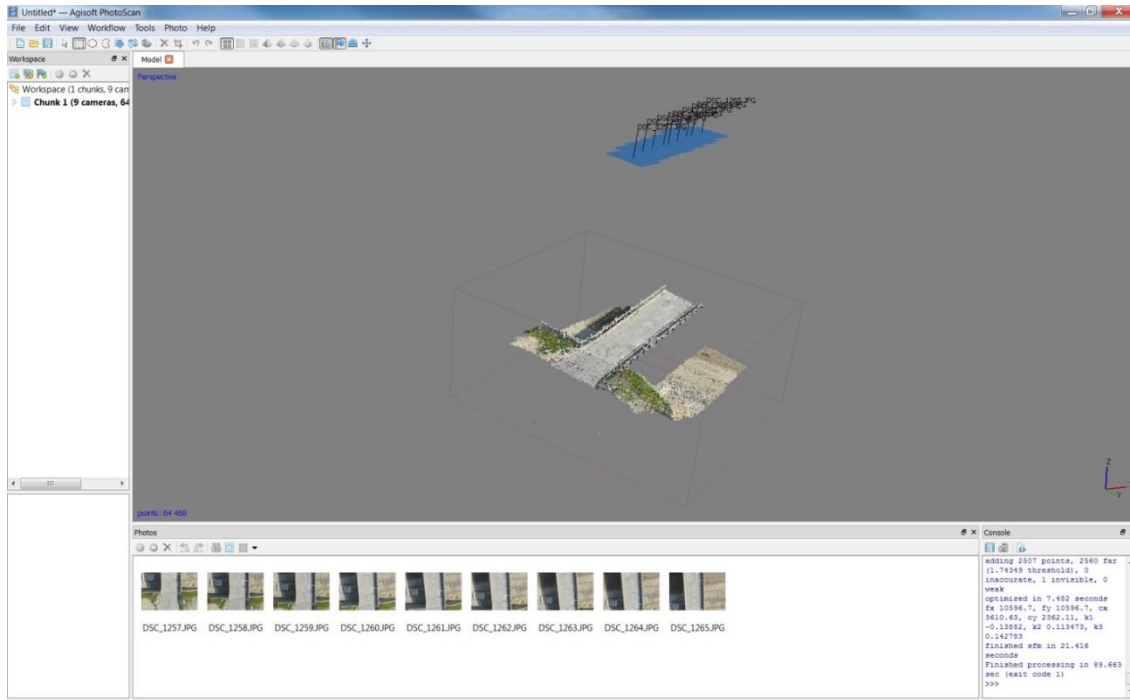


**Figure 5.1 B: A sparse point cloud produced from using the "Align Photos" command.**

After a sparse point cloud is generated, if the user used markers on the ground instead of geotagged imagery, the markers can be added in AgiSoft and the latitude and longitude locations are added into the "Ground Control" panel. If this is done at this point of the processing the user would only have to manually add in the marker once and AgiSoft will automatically place the marker in all other photos that it appears in. The user will have to go through each photo to ensure that the markers have been correctly placed and make adjustments if necessary. If the images are geotagged the user can just proceed to the next step. Also during this step, while using either method, the coordinate system is set by the user. This is done through the ground control panel (Figure 5.1 C).

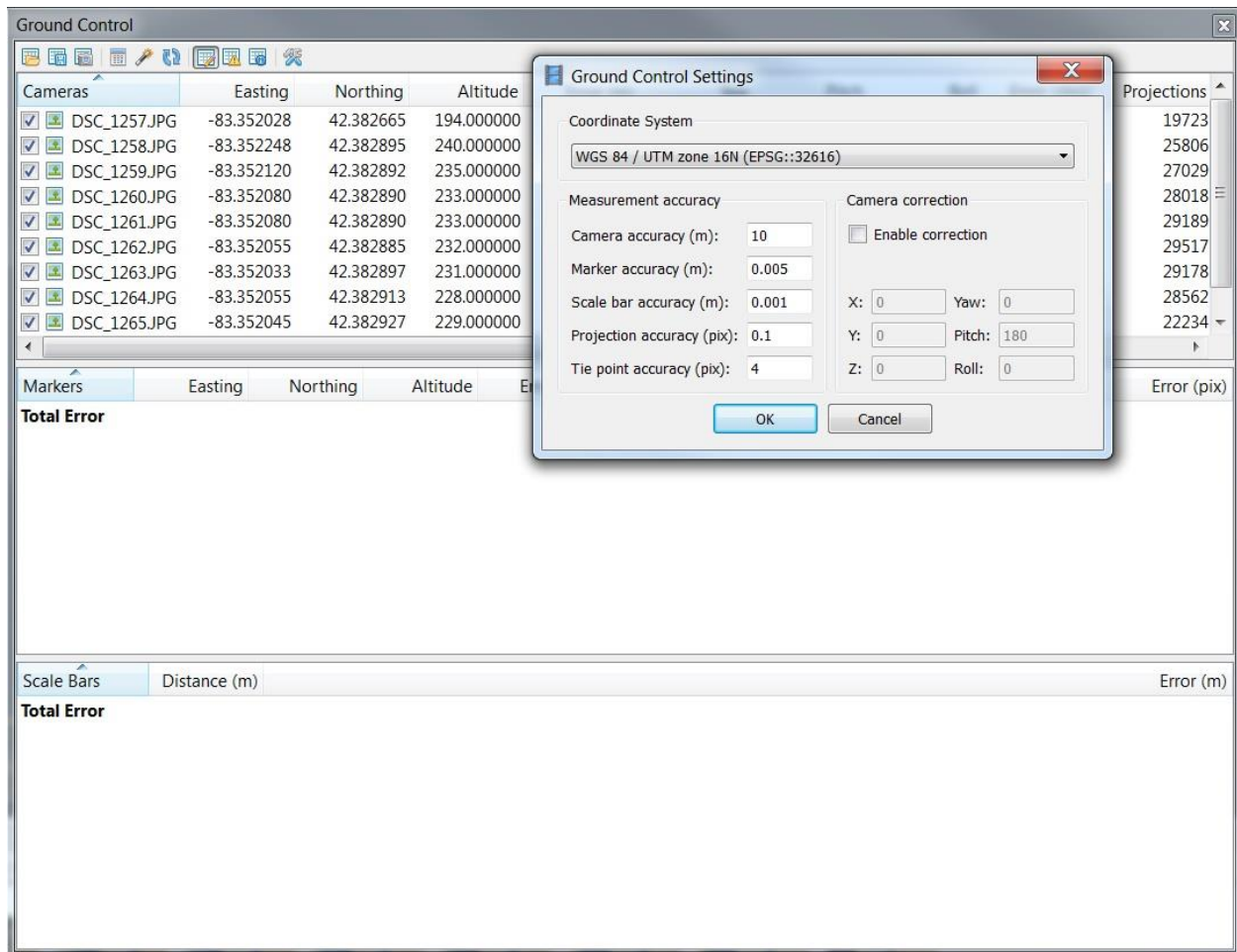


**Figure 5.1 C: Setting the project coordinate system through the ground control panel.**

Building a dense point cloud is the next step in the Agisoft processing. This step takes the sparse point cloud and generates more points based on the scene structure from the photos. Agisoft allows for different levels of quality for the additional points to be generated. The quality in the final point cloud refers to how many additional points are to be generated. This feature is especially helpful as you can scale processing time and power with the quality of the final model.

The final step in the Agisoft processing is building the mesh for the 3D model. This step generates a surface over the point cloud that could be exported as a DEM (Figure 5.1 D). Once the model is completed the user can export an orthoimage and DEM of the bridge deck at any resolution up to the maximum resolution of the 3D model.

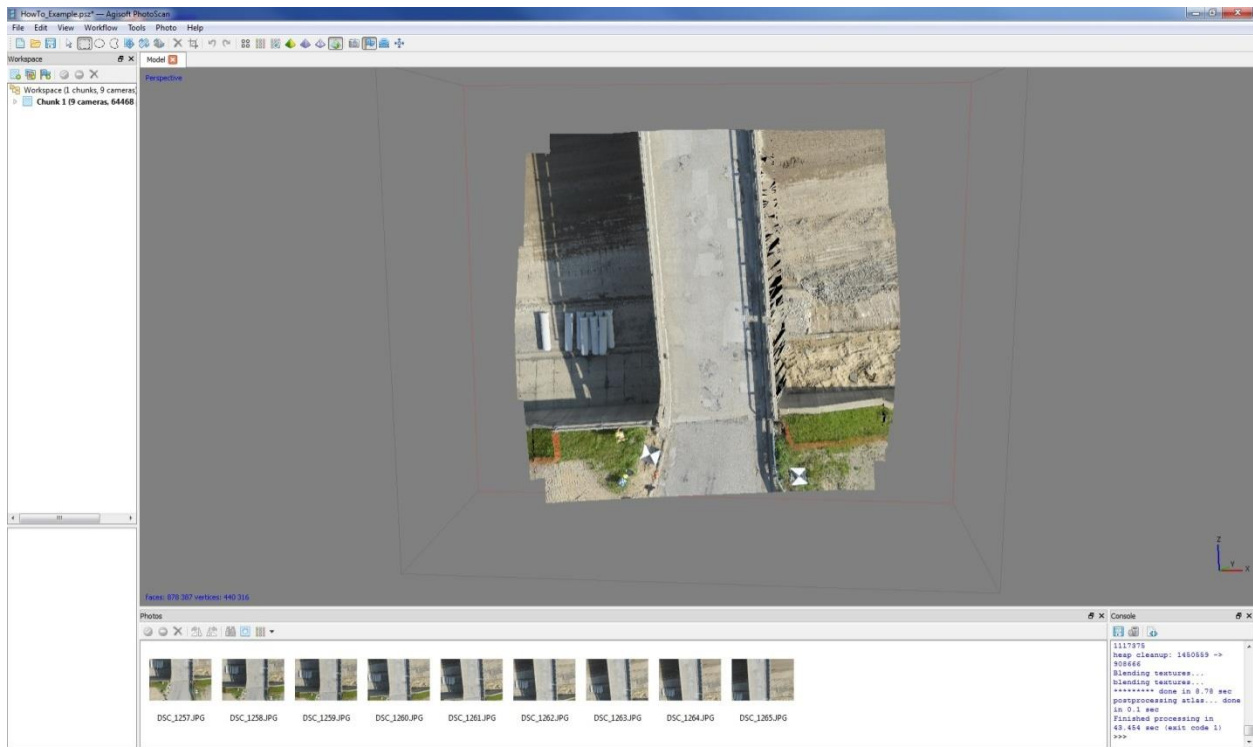


**Figure 5.1 D: A mesh has been generated over the point cloud to make a 3D model.**

### **Automated spall detection**

Spall detection of the bridge decks are done using an automated spall detection algorithm which was developed for previous condition assessment projects. This algorithm uses a DEM of the bridge deck to generate a ArcMap GIS shapefile of the spalls and calculates the area and volume of each. It is written in ArcPy and utilizes ArcGIS tools for the process. Figure 5.1 E shows the Python shell that is used to run the algorithm.

```
*Python Shell*
File Edit Shell Debug Options Windows Help
Python 2.6.5 (r265:79096, Mar 19 2010, 21:48:26) [MSC v.1500 32 bit (Intel)] on
win32
Type "copyright", "credits" or "license()" for more information.

*****
Personal firewall software may warn about the connection IDLE
makes to its subprocess using this computer's internal loopback
interface. This connection is not visible on any external
interface and no data is sent to or received from the Internet.
*****

IDLE 2.6.5
>>> ----- RESTART -----
>>>
Working directory path: E:\3DOBS\Willow_Spall\
Max bridge pixel value: 0.001
Min spall pixel value: 0.00100001
Min spall size: 40
Bridge joint file name: BridgeJoint.shp
DEM Name: Willow_DEM_Final.tif

Ln: 19/Col: 30
```

**Figure 5.1 E: The Python Shell that is used to run the spall detection algorithm.**

Other than the DEM of the bridge deck the user has to create a shapefile of the location of the bridge joints as these small linear depressions are not spalls. The algorithm uses this shapefile to remove the bridge joints from the analysis as they would be included otherwise. Another feature that the user can set is the minimum size of spall (in square centimeters) they want to detect (Figure 5.1 F). This feature restricts the size of spalling detected so that the resulting spall shapefile only represents spalls that are of significant size.

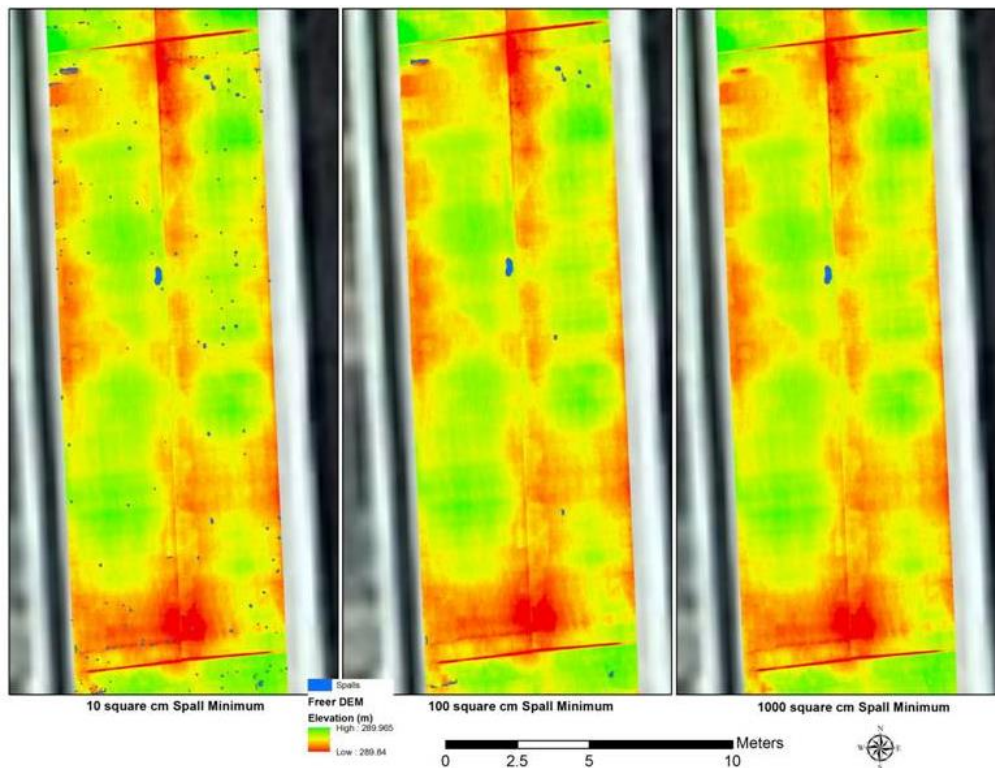


**Figure 5.1 F: Differences in minimum spall sizes as generated from the spall detection algorithm. The first image on the left depicts all spall that are larger than 10 square centimeters (1.6 square inches), then 100 square centimeters (15.5 square inches), then 1000 square centimeters (155 square inches) All of the images are of the same location on Freer Road near Chelsea, MI.**

### Referencing thermal imagery

After the thermal imagery is collected it is georeferenced in ArcGIS so that it lines up with the optical data. Unlike the optical images collected with the Nikon D800 the thermal imagery is not geotagged. The imagery is brought into ArcMap and using the "Georeferencing Toolbar" can be referenced to the orthoimage that was generated from AgiSoft. For this method five common points are selected between the thermal image and the orthoimage (one in each corner and one in the middle) for a proper referencing. Once the points are created the thermal is aligned with the corresponding location on the orthoimage and it is assigned the same coordinate system as well.

Once all of the thermal images are georeferenced they are mosaiced together into a single geotif. This is completed using the "Mosaic to new Raster" tool in ArcMap. After all of the images are mosaiced, a complete thermal image of the bridge deck is referenced to the same location as the data and output from the optical collection.